Materials Today Advances 6 (2020) 100054

Contents lists available at ScienceDirect

Materials Today Advances

journal homepage: www.journals.elsevier.com/materials-today-advances/

Two-dimensional materials as anodes for sodium-ion batteries

Y.-M. Chang [a], H.-W. Lin [a], L.-J. Li [b, c, **], H.-Y. Chen [a, *]

[a] Department of Materials Science and Engineering, National Tsing Hua University, 101, Sec. 2, Kuang-Fu Road, Hsinchu 30013, Taiwan
[b] Physical Science and Engineering Division, King Abdullah University of Science and Technology, Saudi Arabia
[c] School of Materials Science and Engineering, University of New South Wales, Australia

ARTICLE INFO

Article history:
Received 1 November 2019
Received in revised form
4 January 2020
Accepted 8 January 2020
Available online 4 March 2020

Keywords:
Graphene
Transition metal sulfides/selenides
Phosphorene/metal phosphides
MXene
In situ analysis

ABSTRACT

Sodium-ion batteries (NIBs) are considered as promising alternatives to lithium-ion batteries (LIBs) especially in large-scale energy storage systems of renewable energy owing to their potentially low production cost. In view of the larger ionic size of Na ions than Li ions, the commercial graphite anode in LIBs is not suitable for NIBs. To achieve NIBs with a high energy density, various anode materials have been studied in recent years. Among these, two-dimensional (2D) materials have attracted considerable attention on account of their unique 2D-layered structure with infinite planar lengths; these materials provide short paths for sodium-ion transportation and large surface areas for sodium ion adsorption. Furthermore, some 2D materials exhibit a high electronic conductivity (e.g. graphene and metal selenide), which also aids in increasing the capacity and enhancing the rate performance. This review provides an insight into the recent progress in 2D anode materials in NIBs, including graphene and its derivatives, transition metal sulfides/selenides, phosphorene/metal phosphides, transition metal carbides/nitrides (MXene), and other graphene-like elemental analogs (silicene, germanene, stanene, and borophene). Moreover, a series of *in situ* characterization techniques, which have been utilized to investigate the fundamental sodium storage mechanism of the aforementioned 2D anode materials, are explained in-depth in this paper. This review is focused on providing a pathway for comprehending the electrochemical properties and methods to study the sodium storage mechanism of 2D anode materials for further research.

1. Introduction

Lithium-ion batteries (LIBs), with a high energy density, have been widely utilized in portable electronics and electric vehicles since the 1990s [1–4]. Recently, large-scale LIBs, which can be linked to sustainable energy sources, such as solar and wind power, have been introduced to the market. Although LIBs are currently the leading technology for energy storage, the dearth of lithium (~20 ppm in the earth's crust) [5] and their high cost are the main issues that may limit their applications in large-scale energy storage systems [5–8]. Moreover, most of the lithium resources are found in a few areas, such as South America, North America, Australasia, Russia, and China [9]. To develop the LIB market, the foregoing as well as the unsteady supply and increasing price of lithium are the potential risks that other countries would have to accept. As a result, various investigations on new types of batteries have emerged. Relative to the aforementioned, the substantial abundance of sodium on the earth's crust (~2.5%) and its practically unlimited availability in seawater have extremely reduced its cost as compared with lithium. Sodium has similar electrochemical properties as lithium; accordingly, Na-ion batteries (NIBs) have recently been regarded as a promising alternative to LIBs particularly for large-scale energy storage systems [5]. The higher standard reduction potential of Na^+/Na than Li^+/Li ($\Delta E^0 = 0.33$ V) [7] and the heavier atomic mass as well as the larger ionic radius of Na ions have resulted in the lower energy density of NIBs than LIBs; nonetheless, NIBs still perform an important function in large-scale applications because of their cost advantage over LIBs [7].

Based on the knowledge of LIBs, several NIB anode materials, including carbonaceous materials [7,8,10–12], metal oxides/sulfides [12–23], sodium alloys [24–33], phosphorus [24], phosphides [25], and organic compounds [37,38], have been studied in recent years. Most anode materials exhibit a low initial Coulombic efficiency, low specific capacity, and poor cycling stability. These

* Corresponding author.
** Corresponding author.
E-mail addresses: l.li@unsw.edu.au (L.-J. Li), hanyi.chen@mx.nthu.edu.tw (H.-Y. Chen).

https://doi.org/10.1016/j.mtadv.2020.100054

problems need to be overcome in order to achieve a high NIB energy density for large-scale energy storage systems.

After the discovery of graphene in 2004, two-dimensional (2D) materials with atomically thin layers, which are stacked *via* van der Waals forces, have drawn considerable attention; subsequently, they have been widely developed for different applications, such as transistors, catalysts, and energy storage systems [26–28]. Various 2D materials have been extracted by exfoliation or directly synthesized, including graphene and its derivatives [29–33], transition metal dichalcogenides [34,35], transition metal carbides/nitrides (MXene) [36,37] and other graphene-like elemental analogs (black phosphorene [38], silicene [39,40], and borophene [41]). These materials have also been reported as high-performance NIB anodes.

Two-dimensional materials exhibit an ultrathin atomic/molecular layered structure with infinite planar lengths and more exposed interior atoms, and they exhibit tunable chemical and physical properties through the control of defects [26–28]. The large surface area and open structure of 2D materials not only increase the contact area between the active materials and the electrolytes but also reduce the length for the diffusion of Na ions; therefore, an electrode with 2D materials provides a higher theoretical capacity than its bulk form. Two-dimensional materials are stacked by weak van der Waals forces and exhibit good mechanical flexibility; thus, they can accommodate large Na ions and considerable volume changes during the sodiation/desodiation processes. The electronic conductivity of 2D materials ranges from that of insulators to superconductors. Two-dimensional materials with high electronic conductivity can provide both large capacity and good structural stability for NIBs. Although 2D materials have several extraordinary advantages, certain impediments have to be overcome before they can be utilized in NIBs; these include their complex synthetic processes, indistinct sodiation/desodiation mechanism, and severe layer-stacking and aggregation problems [26–28]. Comprehending the charge storage mechanism of 2D anodes in NIBs is important for optimizing the battery performance. Recently, various *in situ/operando* techniques have been applied to investigate the sodiation/desodiation mechanism of 2D materials.

In this article, a comprehensive review of the recent progress in the synthesis and electrochemical performance of 2D materials in NIB anodes is presented, and the fundamental studies of their sodiation/desodiation mechanism *via* different *in situ/operando* characterization techniques are described, as shown in Fig. 1. At the end of the paper, the conclusions and future perspectives related to the major problems and opportunities in using 2D materials are summarized. The review provides detailed discussions enabling in-depth understanding and rational design of 2D NIB anode materials.

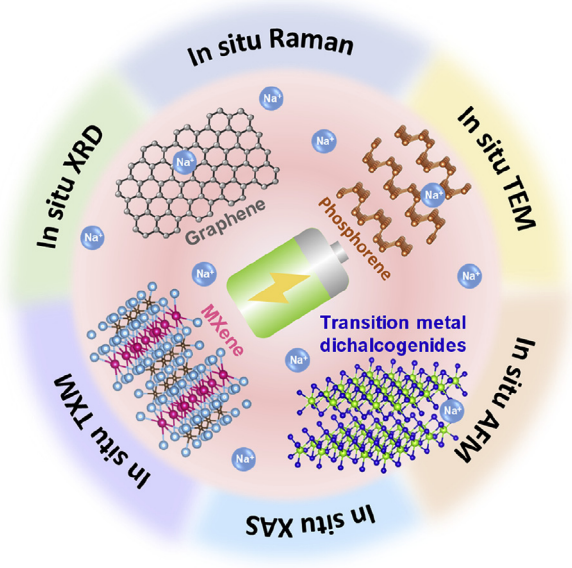

Fig. 1. Schematic overview of 2D materials used for sodium-ion battery anodes and the fundamental studies of their sodiation/desodiation mechanism *via* different *in situ/operando* characterization techniques.

2. Overview of 2D anode materials

2.1. Graphene and its derivatives

Carbon materials have been widely used as anodes in LIBs; in particular, graphite as a commercial anode material for LIBs has an extraordinary electrochemical performance. Sodium ions, however, are approximately 55% larger than lithium ions, making them difficult to locate sufficiently large interstitial sites. It has been proved that graphite is not suitable for NIBs because the sodium ion is impractical to intercalate with graphite; this results in a low capacity [42]. Other carbonaceous materials have been considered including carbon fiber [43], carbon black [44], carbon hollow sphere [45], hard carbon [10], and hollow carbon wires [46]. Carbonaceous materials with two-dimensional structures are also regarded as potential materials for energy storage devices; they have a considerable contact with the electrolyte and exhibit an impressive capacity for transporting electron/sodium ions because of their unique structures. Apart from these, they facilitate strain relaxation which is beneficial during the battery operation [30,47,48].

In 2013, Wang et al. [49] first proposed reduced graphene oxide (rGO) nanosheets for application in NIBs. The sheets exhibit a high capacity of 140 mA h/g at 0.2 C (40 mA/g) with a long cycling life that exceeds 1,000 cycles; they have a remarkable rate capability which provides a reversible capability of 95.6 mA h/g at a considerably high current rate of 5 C (1,000 mA/g). The nanosheet structure could reduce the diffusion length of sodium ions and exhibit an exceptional performance. Graphene, as a carbonaceous 2D material, has gained attention because of its high surface area, superior conductivity, and wide electrochemical window [50,51]. The layer of graphene, however, restacks because of its high surface energy, which limits its application in NIBs [32,52,53]. The most common technique to improve the electrochemical performance of graphene is the incorporation of heteroatoms, such as nitrogen, sulfur, phosphor, and boron. Among these, nitrogen-doped carbon is the most widely investigated, where the nitrogen could enhance electronic conductivity and surface wettability and thus improve the battery performance. Wang et al. [29] synthesized 2D porous N-doped carbon sheets based on the polypyrrole-functionalized graphene that exhibits a highly reversible capacity (349.7 mA h/g at 50 mA/g), good cycling stability of more than 260 cycles, and good rate capability (50 mA h/g, even at a considerably high current density of 20 A/g). A similar strategy is widely used in several works [29–33]. Sulfur-doping is another common approach to improve the properties of 2D materials; it enlarges the interlayer distance and provides more active sites that increase the reaction kinetics and capacity of 2D materials [31,32,54]. The recent work by Quan et al. [55]shows that remarkable electrochemical properties are achieved when graphene is synthesized by the solvothermal method, where the solvothermal graphene exhibits a high degree of disorder, and sulfur-doping was conducted from dimethyl sulfoxide *via* a modified thermal process. The interlayer distance of sulfur-doped solvothermal-synthesized graphene (S-SG) (Fig. 2a) is

significantly larger (~0.41 nm) than that of graphite (~0.34 nm). The S-SG exhibits a remarkably high capacity of 380 mA h/g after 300 cycles at 100 mA/g and an excellent rate performance of 217 mA h/g at 3,200 mA h/g, as shown in Fig. 2b. Additionally, the cycling performance is extraordinary at 2.0 A/g during 1,000 cycles with no capacity fade. Except N and S-doped materials, boron is another ideal candidate for graphene functionalization because it has low electronegativity and an atomic radius similar to carbon [56,57]. In 2016, Wang et al. [57] proposed a boron-functionalized rGO (BF-rGO), which features expanded interlayer spaces and a defected-rich structure, by using a gentle fabrication method (Fig. 2c). The BF-rGO delivers a reversible capacity of 280 mA h/g and a considerable retention of 89.4% after 5,000 cycles at 1,000 mA/g, as presented in Fig. 2d.

Another technique implemented by Xu et al. [58] is the synthesis of 3D porous N-doped graphene nanosheets (Fig. 2e). The well-defined porosity, large surface area, and enlarged lattice spacing coupled with the N-doping-induced defects make the 3D mesoporous graphene attain a higher capacity of 1,057 mA h/g at a current density of 250 mA/g, as shown in Fig. 2f. The cycle retention of graphene, however, does not increase with this design, and the rate capability is insufficient because the capacity to change from high to low rate is irreversible.

The battery performances of graphene and its derivative in NIBs are listed in Table 1. In summary, the 2D carbonaceous materials with heteroatom-functionalization could exhibit good cycle stability. However, the low capacities resulting from the intercalation mechanism limit their application in NIBs. Meanwhile, they typically show a lower 1st Coulombic efficiency which indicates the large capacity loss of the initial discharge/charge capacities. This is owing to the decomposition of the electrolyte, the formation of a solid electrolyte interphase (SEI) layer due to the large surface area, and the irreversible reaction between sodium ions and the functional groups of the graphene [58]. In view of this, because of the flexibility of 2D carbonaceous materials, they are most commonly used as additives to reduce the volume expansion of other active materials.

2.2. Transition metal sulfides/selenides

The use of metal sulfides/selenides (MXs), such as SnS_2 for achieving high capacity and long cycling life in LIBs, has been reported since the 1970s [60]. Numerous studies have also focused on the application of MXs in NIBs, and it has been found that MXs offer higher theoretical capacities *via* conversion and/or alloying mechanisms [35]. However, the voltage plateau change is one major issue for MX materials. For instance, it has been proved that 2H−MoS_2 undergoes an irreversible process to the 1T-MoS_2 in the first cycle by *in operando* XRD detection [61] which leads to the low Coulombic efficiency. Furthermore, the voltage hysteresis is

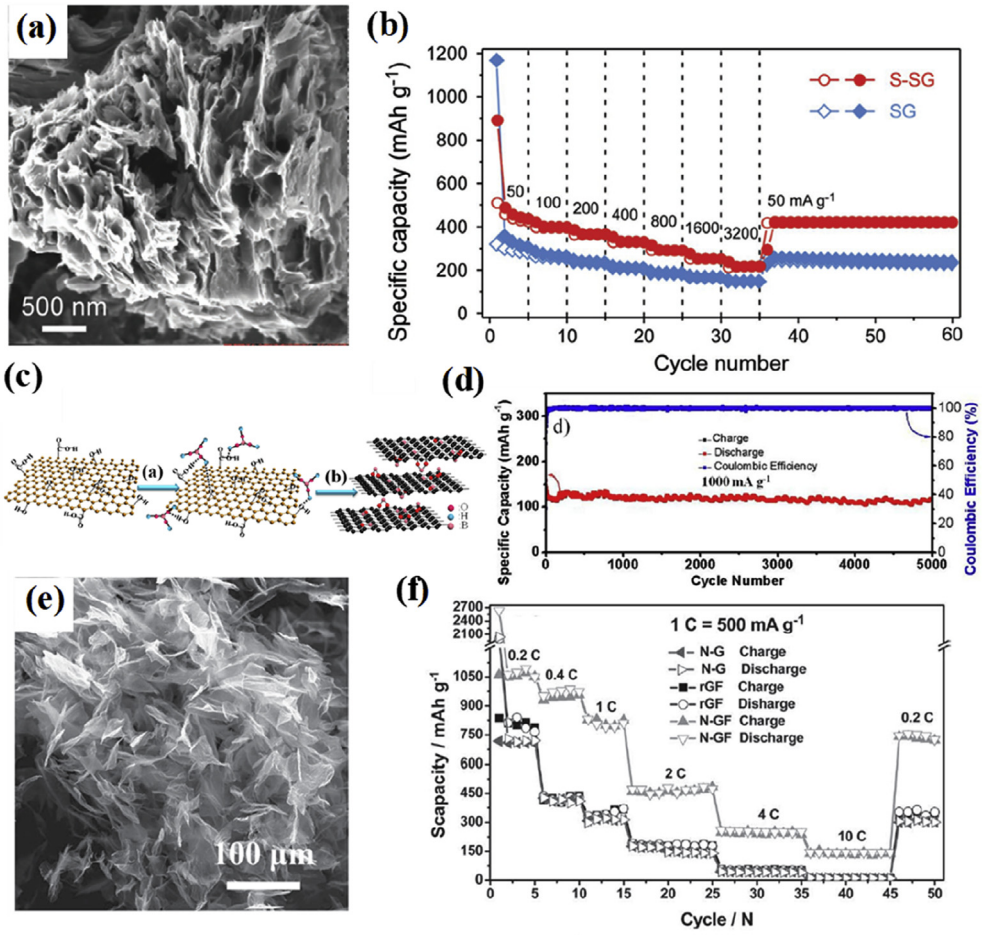

Fig. 2. (a) SEM image of S-doped graphene [55]. Reprinted with permission, copyright 2016, American Chemical Society. (b) Rate performance of S-doped graphene [55]. Reprinted with permission, copyright 2016, American Chemical Society. (c) Illustration of boric acid-functionalized rGO [57]. Reprinted with permission, copyright 2018, Wiley-VCH Verlag GmbH & Co. KGaA. (d) Long-life cycling stability of BF-rGO at 1,000 mA/g [57]. Reprinted with permission, copyright 2018, Wiley-VCH Verlag GmbH & Co. KGaA. (e) SEM image of graphene foam. (f) Rate performance of N-doped graphene foam [58]. Reprinted with permission, copyright 2016, John Wiley and Sons.

Table 1
Electrochemical performance of selected graphene and its derivative anode materials for Na-ion batteries.

Materials	Morphology	Electrolytes	1st Coulombic efficiency (%)	2nd sodiation capacity (mAh/g)	Cycling retention	Ref.
N-doped carbon nanosheets	Nanosheets	1 M $NaPF_6$ (in EC:DEC = 1:1 w/w)	34.9	323 (100 mA/g) ~40 (5 A/g)	~40% @ 50 mA/g (after 200 cycles)	[29]
rGO	Nanosheets	1 M $NaClO_4$ in PC	–	217 (40 mA/g) 96 (1 A/g)	45.0% @ 40 mA/g (after 1,000 cycles)	[49]
Dopamine-derived N-doped carbon sheets	Nanosheets	1 M $NaClO_4$ (in EC:PC = 1:1 v/v)	26.4	212 (100 mA/g) 84 (5 A/g)	~50% @ 200 mA/g (after 600 cycles)	[30]
S-doped graphene	Nanosheets	1 M $NaPF_6$ (in EC:DMC = 1:1 v/v)	57.4	262 (100 mA/g) 83 (5 A/g)	~83% @ 5 A/g (after 100 cycles)	[59]
N-doped carbon sheets	Nanosheets	1 M $NaClO_4$ + 5% FEC (in EC:DMC = 1:1 v/v)	59.7	302 (56.25 mA/g) 32 (11.25 A/g)	~93% @ 56.25 mA/g (after 100 cycles)	[33]
B-doped rGO	Nanosheets	1 M $NaClO_4$ + 5% FEC (in EC:DEC = 1:1 v/v)	37	~190 (100 mA h/g) 123 (1 A/g)	89.4% @ 1,000 mA·h/g (after 5,000 cycles)	[57]
S-doped N-rich carbon nanosheets	Nanosheets	1 M $NaClO_4$ (in EC:PC = 1:1 v/v)	43.8	300 (100 mA/g) 150 (5 A/g)	~100% @ 1 A/g (after 1,000 cycles)	[31]
N and S-doped graphene nanosheets	Nanosheets	1 M $NaClO_4$ + 2% FEC (in EC:DEC = 1:1 v/v)	53.3	313 (100 mA/g) 169 (5 A/g)	82% @ 1 A/g (after 1,200 cycles)	[32]
S-doped graphene	Nanosheets	1 M $NaClO_4$ + 5% FEC (in EC:PC = 1:1 v/v)	55.6	398 (100 mA/g) 217 (3.2 A/g)	~80% @ 100 mA/g (after 300 cycles)	[55]
N-doped graphene	3D graphene foam	1 M $NaPF_6$ (in EC:DEC = 1:2 v/v)	42.6	1,057 (250 mA/g) 138 (5 A/g)	~69.7% @ 500 mA/g (after 150 cycles)	[58]

another reason for the voltage plateau change which usually can be observed during the conversion and alloying reactions [62,63]. The voltage hysteresis is attributed to cracks and subsequent SEI formation, phase transition, internal resistance, polarization, concentration gradient of sodium ions, and mechanical stresses, etc. [62,64]. These voltage plateau changes always lead to a low Coulombic efficiency and inadequate cycling performance. Another problem is caused by sodium sulfides, which are the products of the conversion reaction between the sodium and metal sulfides. Sodium polysulfides would react with carbon-ester-based electrolytes or dissolve in ether-based and carbon-ester-based electrolytes; thus, safety issues and capacity loss have to be considered [35,65,66]. Finally, the conversion reaction always occurs with large volume expansion; a 50–150% volume change occurs in sulfide-based materials in NIBs [67,68]. To achieve a better electrochemical performance for the sodium-ion storage system, the aforementioned problems should be resolved.

Thus far, various metal sulfides have been reported such as Sb_2S_3 [69–71], MoS_2 [72–78], WS_2 [79,80], SnS_2 [81–86], SnS [22,87–92], FeS [93,94], FeS_2 [95,96], MnS [97], VS_2 [98,99], VS_4 [100], CoS [101–104], Cu_2S [105], and NiS_2 [106]. The most common approach to relieve the problems mentioned above is through carbon coating or mixing; in this way, volume expansion could be significantly reduced. For instance, Choi et al. [73] prepared 3D MoS_2–graphene microspheres with a long cycling performance and a good rate performance (Fig. 3a). The current density ranged from 1 to 10 A/g and showed a reversible capacity back to 1 A/g (Fig. 3b). The strategy of this study is to design a novel few-layer MoS_2 composite on 3D graphene microspheres. The usage of 3D graphene is better than that of 2D nanosheets because it results in less aggregation and provides large surface area, novel physical properties, and structural stability. Porous 3D graphene sheets have been reported to limit the volume change and allow the easy migration of electrolytes [107–113].

The usage of few-layer nanosheets is therefore another approach to increase the performance of the batteries. Zhou et al. synthesized VS_2 with a thickness of approximately 9 nm *via* a facile solvothermal method; VS_2 nanosheet assemblies are formed in the range of 500 nm–1 μm with approximately 10 atomic layers, as shown in Fig. 3c [99]. These sheets thus provide short diffusion paths for sodium ions and exhibit an exceptional performance; even at less than 1 and 2 A/g, they still exhibit capacities of 550 and 400 mA h/g, respectively, as shown in Fig. 3d. Another common structure design for enhancing electrochemical performance is the yolk–shell [94,96] or hollow structure [97,104,114]. This type of structure has a larger surface area than its spherical counterpart with an identical volume, which provides more active sites for sodium ion and electrolyte [115,116]. Recently, Wang et al. reported their study of CoS_2 multishelled nanoboxes derived from metal–organic frameworks (MOFs) (Fig. 3e) [104]. In this structure, the gap between the adjacent shells can overcome the large volume expansions during the sodiation/desodiation process. Hence, the triple-shelled CoS_2 exhibits a remarkable performance after 100 cycles and at a current density of 200 mA/g, and its capacity remains at 95% and rate performance (which could recover from a change of 5 to 0.1 A/g) is good as shown in Fig. 3f.

Recently, the use of bimetallic sulfides, such as Co_9S_8/ZnS [114], $Co_{0.5}Fe_{0.g}S_2$ [66], and $(Ni_{0.3}Co_{0.7})_9S_8$ [117], has been investigated, and such a strategy could provide abundant phase boundaries during the sodiation/desodiation processes. Along with the hollow structure, bimetallic sulfides provide small crystalline domains, which could preclude deep solid-state diffusion and enhance the pseudocapacitance effect [118–120]. When compared to monometallic sulfides, bimetallic sulfides exhibit a higher electronic conductivity and multiple redox reactions, which can significantly enhance the electrochemical performance [121]. The battery performances of metal sulfides in NIBs are summarized in Table 2.

Compared to metal sulfides, metal selenides have similar layered structures, lower theoretical capacities, and better electrical conductivity [126]. Accordingly, they have been investigated in recent years. Among the most thoroughly investigated materials is $MoSe_2$. Compared with MoS_2, $MoSe_2$ possesses a larger interlayer and smaller band gap, which would lead to a better Coulombic efficiency and rate capability [34]. Numerous studies, however, indicate that the capacity of $MoSe_2$ (i.e. 450 mA h/g) is not ideal [127–129]. In 2016, Tang et al. reported the creation of $MoSe_2$@OA-PDA (i.e. $MoSe_2$ fabricated by oleic acid (OA)-functionalized synthesis and polydopamine (PDA) stabilization–carbonization strategy) (Fig. 4a) [130]. This material has a remarkable performance: 545 mA h/g (this is significantly higher than 450 mA h/g) at a current density of 0.1 A/g. Its rate performance is also significant: as shown in Fig. 4b–d, the capacities are 545 mA h/g at 0.1 A/g and 367 mA h/g at 5 A/g; it can also recover from the current density of 5 to 0.1 A/g.

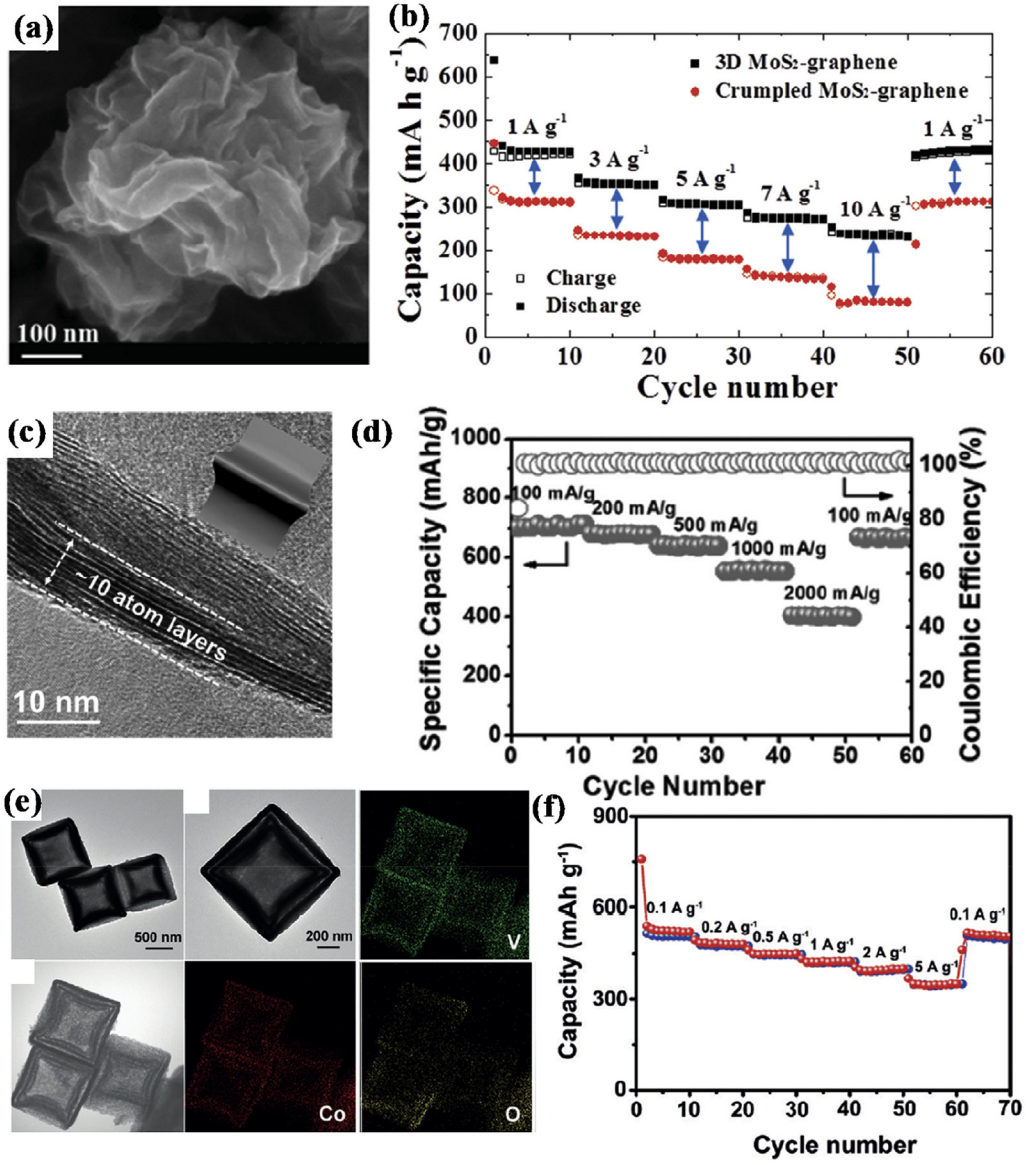

Fig. 3. (a) SEM image of 3D MoS_2-graphene [73]. Reprinted with permission, copyright 2015, John Wiley and Sons. (b) Rate performance of 3D MoS_2-graphene [73]. Reprinted with permission, copyright 2015, John Wiley and Sons. (c) TEM image of VS_2 nanosheet assemblies [99]. Reprinted with permission, copyright 2017, John Wiley and Sons. (d) Rate performance of VS_2 NSCS [99]. Reprinted with permission, copyright 2017, John Wiley and Sons. (e) TEM images and element mapping of CoS [104]. Reprinted with permission, copyright 2019, John Wiley and Sons. (f) Rate performance of multishelled CoS [104]. Reprinted with permission, copyright 2019, John Wiley and Sons.

Multimetallic selenides have also gained widespread interest as materials for sodium-ion storage systems [131,133,134]. Ali et al. reported a binary-metal selenide, Fe_2CoSe_4, which possesses a "metal-like" conductivity [131]. With this property, Fe_2CoSe_4 exhibits an excellent rate capability, as shown in Fig. 4e–f. At current densities of 0.5 and 32 A/g, it exhibits reversible capacities of 816.3 and 400.2 mA h/g, respectively. Additionally, after 5,000 cycles, Fe_2CoSe_4 remains with a capacity of 350 mA h/g. Another strategy is to combine metal sulfides with metal selenides for achieving a high electrical conductivity. Tang et al. prepared ternary $SnSe_{0.5}S_{0.5}$ by a facile polyol method [132]; $SnSe_{0.5}S_{0.5}$ shows an outstanding capacity of 612 mA h/g at a current density of 0.2 A/g and ~86% cycle retention after 100 cycles (Fig. 4g). The performances of NIB with metal selenides are summarized in Table 3.

Nanostructured, carbon-modified, and multi-element optimized metal sulfides/selenides have been widely researched. However, these materials have relatively high reaction potentials, which is not ideal for anode materials. In view of their short diffusion length and remarkable conductivity, it is probable that MXs will be used as the electrodes for pseudocapacitors or Na-ion capacitors in the future.

In Tables 2 and 3, the same materials might exhibit different capacities. To better understand the influence of morphology, Table 4 compares the different structure designs and electrochemical performances of MoS_2 and SnS_2. The corresponding morphologies are shown in Fig. 5. This obviously shows that the nanosized materials exhibit higher capacities than the bulk materials or restacked microplates. By decreasing the particle size, it usually shows the larger capacities and better cycle retentions because of the large surface area for reaction and a higher tolerance for volume change during the repeated sodiation/desodiation processes. The SnS_2 nanowall array electrode exhibited a superior sodium storage capability [86]. It provided a high capacity up to 730 mA h/g at 100 mA/g and 474 mA h/g at 5 A/g, indicating an

Table 2
Electrochemical performance of selected metal sulfide anode materials in Na-ion batteries.

Materials	Morphology	Electrolytes	1st Coulombic efficiency (%)	2nd sodiation capacity (mA h/g)	Cycling retention	Ref.
Sb_2S_3/rGO	Nanoparticles	1 M $NaClO_4$ + 5% FEC (in EC)	65.7	730 (50 mA/g) 520 (3 A/g)	>95% @ 50 mA/g (after 50 cycles)	[69]
Sb_2S_3/graphite	–	1 M $NaClO_4$ + 5% FEC (in EC:PC = 1:1 v/v)	84	733 (100 mA/g) 536 (10 A/g)	99.1% @ 1 A/g (after 100 cycles)	[70]
Sb_2S_3/S-doped graphene	Nanoparticles/nanosheets	1 M $NaClO_4$ + 5% FEC (in PC)	77.9	792.8 (30 mA/g) 591.6 (5 A/g)	83.0% @ 2 A/g (after 900 cycles)	[71]
MoS_2	Nanoflowers	1 M $NaCF_3SO_3$ (in DEGDME)	90.1	300 (1 A/g) 195 (10 A/g)	–	[72]
MoS_2/graphene	Nanospheres	1 M $NaClO_4$ + 5% FEC (in EC:DMC = 1:1 v/v)	71.9	427 (1 A/g) 234 (10 A/g)	84% @ 1.5 A/g (after 600 cycles)	[73]
MoS_2/PEO	Nanosheets	1 M $NaCF_3SO_3$ (in DEGDME)	~83	185 (50 mA/g) 112 (1 A/g)	67.6% @ 50 mA/g (after 70 cycles)	[74]
MoS_2/graphene	Nanoplates/nanosheets	1 M $NaClO_4$ (in EC:PC = 1:1 v/v)	~41	702 (20 mA/g) 352 (640 mA/g)	49.0% @ 20 mA/g (after 100 cycles)	[122]
MoS_2	Ultrathin Nanosheets	1 M $NaClO_4$ (in EC:PC = 1:1 v/v)	40	510 (40 mA/g) 320 (320 mA/g)	72% @ 40 mA/g (after 100 cycles)	[75]
MoS_2/SWCNT	Nanosheets	1 M $NaClO_4$ (in EC:DEC = 1:1 v/v)	~57	437 (50 mA/g) 192 (20 A/g)	~70% @ 500 mA/g (after 1,000 cycles)	[76]
MoS_2/MWCNT/rGO	3D networks	1 M $NaClO_4$ + 5% FEC (in EC:PC = 1:1 v/v)	74	648 (100 mA/g) 381 (2 A/g)	~67% @ 2 A/g (after 500 cycles)	[77]
MoS_2/MOF-derived N-doped carbon	Nanosheets/nanowall	1 M $NaClO_4$ + 5% FEC (in EC:DMC = 1:1 v/v)	52	660 (100 mA/g) 235 (2 A/g)	~94.7% @ 200 mA/g (after 100 cycles)	[93]
MoS_2/carbon	Nanoparticles/nanofiber	1 M $NaClO_4$ + 5% FEC (in EC:DMC = 1:1 v/v)	50	500 (100 mA/g) 210 (20 A/g)	~65% @ 1 A/g (after 2,600 cycles)	[78]
WS_2-decorated rGO	Nanosheets/microspheres	1 M $NaClO_4$ + 5% FEC (in EC:DMC = 1:1 v/v)	56	404 (100 mA/g) 287 (900 mA/g)	93.8% @ 200 mA/g (after 200 cycles)	[79]
WS_2/CNT–rGO	Scaffold network	1 M $NaPF_6$ + 2% FEC (in EC:DEC = 1:1 v/v)	25.1	311.4 (100 mA/g) 47.2 (10 A/g)	~76% @ 200 mA/g (after 100 cycles)	[80]
SnS_2/rGO	Nanocrystalline	1 M $NaClO_4$ + 5% FEC (in PC)	66.7	600 (50 mA/g) 340 (2 A/g)	–	[82]
SnS_2/rGO	–	1 M $NaClO_4$ (in EC:DEC = 1:1 v/v)	76.9	671 (100 mA/g) 544 (2 A/g)	97.3% @ 200 mA/g (after 100 cycles)	[81]
SnS_2/graphene	Nanoplates	1 M $NaClO_4$ (in EC:DEC = 1:1 v/v)	~70	650 (200 mA/g) 326 (4 A/g)	95.2% @ 200 mA/g (after 100 cycles)	[83]
SnS_2/rGO	Plate-on-sheet	1 M $NaPF_6$ + 5% FEC (in EC:DEC = 1:1 v/v)	64	582 (200 mA/g) 337 (12.8 A/g)	~75% @ 400 mA/g (after 500 cycles)	[84]
SnS_2	Nanosheets	1 M $NaClO_4$ + 5% FEC (in PC)	59	685 (100 mA/g) 435 (2 A/g)	88.2% @ 100 mA/g (after 50 cycles)	[85]
SnS_2/EDA–rGO	Nanocrystalline/nanosheets	1 M $NaClO_4$ + 5% FEC (in EC:PC = 1:1 v/v)	73	760 (180 mA/g) 250 (11.2 A/g)	85% @ 1 A/g (after 1,000 cycles)	[123]
SnS_2/graphene foam	Branched nanoarray	1 M $NaPF_6$ (in EC:DEC:FEC = 1:1:0.03 v/v/v)	73	910 (200 mA/g) ~420 (10 A/g)	89% @ 200 mA/g (after 200 cycles)	[124]
SnS_2	Nanowall array	1 M $NaPF_6$ + 5% FEC (in EC:DEC:PC = 4:4:2 v/v)	75.3	730 (100 mA/g) 474 (5 A/g)	85% @ 500 mA/g (after 100 cycles)	[86]
Orthorhombic SnS	Nanosheets	1 M $NaClO_4$ + 5% FEC (in EC:PC = 1:1 v/v)	72.2	1,037 (30 mA/g) 308 (7.29 A/g)	–	[22]
SnS/C	Cubic-like/microspheres	1 M $NaClO_4$ + 5% FEC (in EC:DMC = 1:1 v/v)	63	541 (100 mA/g) 280 (5 A/g)	89% @ 500 mA/g (after 50 cycles)	[87]
SnS/rGO + C	–	1 M $NaPF_6$ (in EC:DEC = 1:1 v/v)	78.2	590 (50 mA/g) 458 (500 mA/g)	~88% @ 500 mA/g (after 30 cycles)	[88]
SnS/graphene foam	Nanohoneycomb	1 M $NaPF_6$ (in EC:DEC:FEC = 1:1:0.03 v/v/v)	81	~1,100 (30 mA/g) ~420 (30 A/g)	~88% @ 100 mA/g (after 200 cycles)	[89]
SnS/SnO2 @ graphene	–	1 M $NaClO_4$ + 5% FEC (in EC:DEC = 1:1 v/v)	74.6	729 (30 mA/g) 430 (2.43 A/g)	~73% @ 810 mA/g (after 500 cycles)	[90]
SnS/C	Nanosheets	1 M NaClO4 + 5% FEC (in EC:DMC = 1:1 v/v)	~74	843 (100 mA/g) 43 (3 A/g)	87% @ 100 mA/g (after 100 cycles)	[91]
SnS/N-doped graphene	Nanoparticles/nanosheets	1 M $NaClO_4$ + 5% FEC (in PC)	81	912.5 (100 mA/g) 404.8 (6 A/g)	87.1% @ 2 A/g (after 1,000 cycles)	[92]
FeS/C	Yolk–shell	1 M $NaClO_4$ + 5% FEC (in EC:PC = 1:1 v/v)	70.2	621 (100 mA/g) 452 (2.5 A/g)	67.6% @ 100 mA/g (after 300 cycles)	[94]
FeS/Fe_3C/graphitic C	3D networks	1 M $NaClO_4$ + 5% FEC (in EC:PC = 1:1 v/v)	60	585 (100 mA/g) 292 (5 A/g)	~80% @100 mA/g (after 100 cycles)	[125]

FeS_2	Microspheres	1 M $NaCF_3SO_3$ (in DGM)	~80	250 (200 mA/g) 170 (20 A/g)	~90% @ 1 A/g (after 20 000 cycles)	[95]
FeS_2/C	Yolk–shell nanoboxes	1 M $NaCF_3SO_3$ + 5% FEC (in DEGDME)	61.65	560 (100 mA/g) 403 (5 A/g)	~70% @ 2 A/g (after 800 cycles)	[96]
MnS/rGO	Hollow microspheres/nanosheets	1 M $NaClO_4$ + 2% FEC (in EC:DMC = 4: 6 v/v)	–	350 (100 mA/g) 118 (800 mA/g)	62.0% @ 100 mA/g (after 125 cycles)	[97]
VS_4/rGO	Nanoparticles/crumpled sheet	1 M $NaClO_4$ (in EC:DMC = 1: 1 v/v)	75	341.5 (100 mA/g) 192.1 (800 mA/g)	84% @ 100 mA/g (after 50 cycles)	[100]
VS_2	Nanosheets	1 M $NaClO_4$ (in EC:DEC:FEC = 1:1:0.06 v/v/v)	86	~700 (100 mA/g) 400 (2 A/g)	~90% @ 1 A/g (after 200 cycles)	[99]
VS_2	Flower-like nanosheets	1 M $NaCF_3SO_3$ (in DGM)	93.7	~600 (100 mA/g) 277 (20 A/g)	83% @ 2 A/g (after 700 cycles)	[98]
CoS/rGO	Plate-on-sheet	1 M $NaCF_3SO_3$ (in DEGDME)	93	636 (100 mA/g) 359 (5 A/g)	~88% @ 1 A/g (after 1,000 cycles)	[101]
CoS/graphene	Nanoparticles/nanosheets	1 M $NaCF_3SO_3$ (in DGM)	82	466 (100 mA/g) 210 (10 A/g)	~66% @ 1 A/g (after 200 cycles)	[102]
CoS Stainless steel mesh	Nanosheets	0.8 M $NaPF_6$ (in EC:DEC = 1:1 v/v/v)	62.9	316 (50 mA/g) 196 (1 A/g)	~69% @ 50 mA/g (after 100 cycles)	[103]
CoS	Multishelled nanoboxes	1 M $NaClO_4$ (in EC:DEC = 1:1 v/v)	68	524 (100 mA/g) 346 (5 A/g)	95% @ 200 mA/g (after 100 cycles)	[104]
NiS_2/graphene	Nanoparticles/nanosheets	1 M $NaClO_4$ + 5% FEC (in EC:DMC = 4: 6 v/v)	65	407 (0.1 C) 168 (2 C)	77% @ 0.1 C (after 200 cycles)	[106]
Cu2S	Nanoflakes	1 M $NaPF_6$ (in DGM)	84.9	420 (100 mA/g) 354 (10 A/g)	88.2% @ 5 A/g (after 5,000 cycles)	[105]
Co_9S_8–ZnS/N-doped carbon	Nanocrystal/nanosheets	1 M $NaClO_4$ + 5% FEC (in EC:DMC = 1:1 v/v)	71	542 (100 mA/g) 258.6 (10 A/g)	88% @ 5 A/g (after 500 cycles)	[114]
$Co_{0.5}Fe_{0.5}S_2$	Microspheres	1 M $NaCF_3SO_3$ (in DGM)	–	~395 (50 mA/g) 173 (20 A/g)	–	[66]
$(Ni_{0.3}Co_{0.7})_9S_8$/N-doped CNT/rGO	Nanoparticles/nanosheets	1 M $NaClO_4$ + 5% FEC (in EC:PC = 1:1 v/v)	44.5	481 (25 mA/g) 283 (500 mA/g)	~57% @ 25 mA/g (after 300 cycles)	[117]
MoS_2–Ni_9S_8–C	Microspheres	1 M $NaClO_4$ + 5% FEC (in EC:DMC = 1:1 v/v)	65	462 (100 mA/g) 307 (2 A/g)	91% @ 500 mA/g (after 80 cycles)	[77]
MoS_2–Ni_9S_8	Microspheres	1 M $NaClO_4$ + 5% FEC (in EC:DMC = 1:1 v/v)	76	559 (100 mA/g) 428 (2 A/g)	92% @ 500 mA/g (after 80 cycles)	[77]

excellent rate capability. It also presented a high cycling retention (~85% after 100 cycles). This could be attributed to the structural design and a direct growth process, which enable the fast electron and Na-ion transport and provide stable structure for the sodiation/desodiation processes.

2.3. Phosphorene/metal phosphides

Phosphorus, a naturally abundant and environmentally friendly element, has been considered as another potential candidate for the high power density anode in energy storage systems because Li_3P and Na_3P exhibit a high theoretical capacity, i.e. 2,596 mA h/g [146–148]. A monolayer or few-layer phosphorene can be derived from one of the phosphorus allotropes, black phosphorus (BP), *via* a simple chemical or physical method similar to that employed to obtain graphene layers [146,149,150]. Compared with red phosphorus, phosphorene has weak interlayers bounded by van der Waal's forces; accordingly, it exhibits excellent charge transport properties, high thermal stability, and considerable electrical conductivity [28]. It has a similar layer structure as graphene but has a greater interlayer distance as phosphorus (5.4 Å for black phosphorus vs. 3.2 Å for graphite) [151,152]; accordingly, some studies on its use for LIBs/NIBs have been conducted. In 2015, Hembram et al. reported the first-principle calculations of BP for NIBs [153]. Their work indicated that sodium ions intercalate into phosphorene at low ion concentrations; at high ion concentrations, BP forms alloys with sodium (Fig. 6a). The results further indicate that sodium diffusion on phosphorene is extremely fast, and the energy barrier is low. The study therefore featured a promising anode material for NIBs with superior mobility, good structure stability, and high electronic conductivity [153]. Several studies of BP as an anode for LIBs have been conducted; however, it has been observed that the cycling performance is extremely low [146,154–156].

It is thus evident that the performance of BP for NIBs has to be improved. Sun et al. synthesized a phosphorene–graphene hybrid material to study the sodiation mechanism of phosphorene (Fig. 6b–c) [38]. When the cut-off voltage is controlled and the electrochemical measurement is conducted, the results indicate that the intercalation mechanism only occurs above 0.54 V; below this, the alloying mechanism would be dominated and the cycling stability significantly decreased. Compared with this theoretical study, it has been observed that $Na_{0.17}P$ is formed by intercalating, which considerably agrees with the report. In this study, the theoretical volume expansion is ~500%; the *in situ* TEM shows a volume expansion of 92% (Fig. 6d–f). With a C:P ratio of 2.78:1, the sandwiched phosphorene–graphene hybrid material can exhibit an outstanding specific capacity of 2,440 mA h/g at a current density of 50 mA g^{-1}; this corresponds to an 85% capacity retention after 100 cycles, as shown in Fig. 6g–f. The result shows that the hybrid material has a high capacity, rate capability, and cycle life as an anode for NIBs. Other theoretical calculations have also been studied for other phosphorene-modified 2D materials, such as hexagonal boron nitride (h-BN) and graphene [157,158]. Capped with h-BN, the BP exhibits a minimal diffusion barrier of 0.06 eV, and the volume change is smaller than 2%, which optimizes the degradation of phosphorene [157]. Lee et al. discovered a mechanical buffer by mixing phosphorene and graphene. They found that no C–C bond breaking occurs during the sodiation process, and the graphene layer provides a facile sodium-ion diffusion channel, which contributes to the superior high-cycling properties.

Several metal elements have been introduced as metal phosphides, such as Sn_xP_y (Sn_4P_3 and SnP_3) [25,40,150,159,160], Ni_2P [161], CoP [162,163], and FeP [164,165], because of the severe volume expansion of phosphorus; among these, Sn_4P_3 has been considerably investigated. For example, in 2014, Qian et al. reported

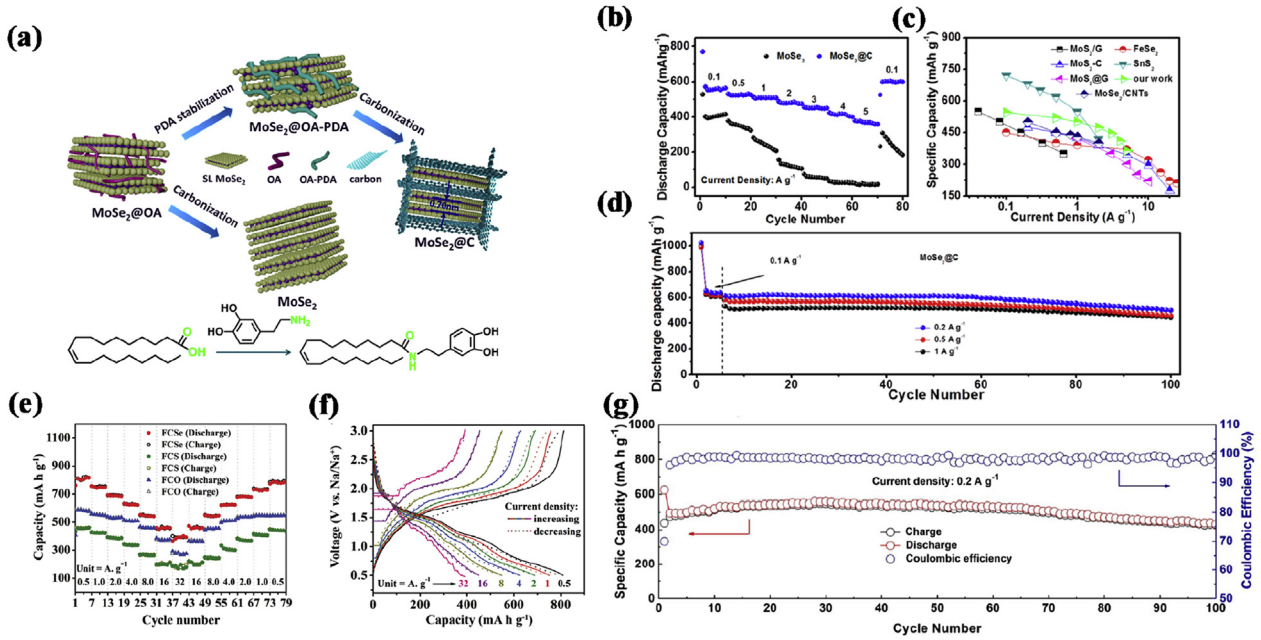

Fig. 4. (a) Synthesis procedure of $MoSe_2$ functionalized by oleic acid and assisted by dopamine [130]. Reprinted with permission, copyright 2016, American Chemical Society. (b) Rate performance of $MoSe_2$@C and $MoSe_2$ [130]. Reprinted with permission, copyright 2016, American Chemical Society. (c) Rate capability of various anodes for NIBs [130]. Reprinted with permission, copyright 2016, American Chemical Society. (d) Cycling stability of $MoSe_2$@C [130]. Reprinted with permission, copyright 2016, American Chemical Society. (e–f) Rate performance of Fe_2CoSe_4 [131]. Reprinted with permission, copyright 2018, John Wiley and Sons. (g) Cycling performance of $SnSe_{0.5}S_{0.5}$ [132]. Reprinted with permission, copyright 2017, Elsevier.

Sn_4P_3 as a graphite-supported synergistic Na-storage material [166]. In this article, the mechanism of tin phosphide is confirmed by *ex situ* XRD analysis. The alloys of Na_3P and $Na_{3.75}Sn$ are formed during the initial sodiation process; however, the CV curve exhibits anodic peaks at 0.3 V and 0.65 V, which indicates the formation of Na and Sn, respectively (Fig. 7a). The irreversible formation of Sn and P leads to their agglomeration, as shown in Fig. 7b, and the mechanism is determined by *ex situ* XRD in Fig. 7c. The design of tin phosphide must therefore be ultra-small; otherwise, the self-aggregation and pulverization of Sn–P would cause the severe degradation of the electrochemical performance [25,159,160].

Metal phosphides are also produced by facile preparation methods, such as ball-milling [163,165,167]. For example, Zhang et al. synthesized a ternary material, Sn_5SbP_3/C, with this method [167]. The high volumetric and gravimetric capacities are contributed by Sn, Sb, and P; the multiple phases create a buffering effect and better electric/ionic conductivity. The specific capacities are 432 and 371 mA h/g after 200 cycles at a current density of 500 and 1,000 mA/g, respectively; these exhibit a good cycle retention of 95%. In this study, however, cracks caused by the volume expansion are also observed after 1,000 cycles as shown in Fig. 7d–e.

The electrochemical performances of the selected phosphorene and metal phosphide anode materials for NIBs are listed in Table 5. In summary, phosphorene exhibits high capacities but suffers the common alloying reaction problems, such as volume expansion, which largely limits its application. To attain the buffering effect, metal phosphide nanoparticles have been introduced to NIBs; nevertheless, the diminishment of the electrochemical performance remains evident during the charge/discharge process.

2.4. MXene

One of the well-known 2D materials is MXene, which is formulated as $M_{n+1}X_nT_x$ (M = Ti, V, etc.; X = C, N; n = 1–3; T_x is the functional termination group, such as –OH, F, and/or O) [170,171]. This material has drawn tremendous interest from scientists because of its high theoretical capacity (351.8 mA h/g) for NIBs and flexible interlayer space capable of handling high rate capability [172,173]. A typical method to synthesize MXene is by selectively etching the A layer out of the $M_{n+1}AX_n$ compound (A is mainly of group IIIA or IVA); the etching solution is usually hydrofluoric acid and a mixture of lithium fluoride with hydrochloric acid [36,37]. The typical morphologies of Ti_3AlC_2 and $Ti_3C_2T_x$ are shown in Fig. 8a–d [36].

Kajiyama et al. published a study pertaining to the sodiation mechanism of a typical $Ti_3C_2T_x$ [36]. The results show that the interlayer distance expanded during the initial sodiation and the interlayer distance remains constant thereafter. To confirm the mechanism, an *ex situ* NMR measurement is employed, as displayed in Fig. 8e. Peak A indicates that the sodium ion is strongly shielded by the solvent molecules; peaks B and C present that the sodium ion is adsorbed on the external surface and edge of the particles and the desolvated Na^+ is intercalated into $Ti_3C_2T_x$, respectively. Solvent molecules therefore penetrate into the interlayer space, which behave as a pillar. In conclusion, the constant interlayer distance leads to a high cycle stability and fast Na^+ diffusion; nevertheless, the practical capacity of pure $Ti_3C_2T_x$ is extremely low. In this study, the stable capacity is approximately 100 mA h/g at a relatively low current density of 20 mA/g.

The face-to-face stacking of the MXene nanosheets limits the practical capacity and rate capabilities [174,175]. To overcome this problem, several strategies have been employed on MXene. Xie et al. reported a porous $Ti_3C_2T_x$ nanosheet (Fig. 8g) for improving electrode/electrolyte interactions and reducing the duration of transportation and diffusion of sodium ions [37]. This exhibits the extraordinary rate capabilities (Fig. 8h). Even at a current density of 100 A/g, its capacity remains at 24 mA h/g. The foregoing demonstrates a super-long cycle life, which could maintain a stable capacity of 189 mA h/g after 1,000 cycles at a current density of 1 A/g (Fig. 8i).

Table 3
Electrochemical performance of the selected metal selenide anode materials for Na-ion batteries.

Materials	Morphology	Electrolytes	1st Coulombic efficiency (%)	2nd sodiation capacity (mA h/g)	Cycling retention	Ref.
$MoSe_2$/graphene	Nanoplates	1 M $NaClO_4$ (in PC)	86	440 mA h/g (0.1 C) 250 mA h/g (1 C)	~83% @ 0.1 C (after 50 cycles)	[128]
$MoSe_2$	Yolk−shell microspheres	1 M $NaClO_4$ + 5% FEC (in EC:DMC = 1:1 v/v)	85	442 mA h/g (100 mA/g) 345 mA h/g (1.5 A/g)	99% @ 200 mA/g (after 50 cycles)	[127]
$MoSe_2$@MWCNT	Nanosheets/multiwalled carbon nanotube	1 M $NaClO_4$ + 5% FEC (in EC:DMC = 1:1 v/v)	74	456 mA h/g (200 mA/g) 385 mA h/g (2 A/g)	~99% @ 200 mA/g (after 90 cycles)	[129]
$MoSe_2$/C	Nanosheets	1 M $NaClO_4$ (in EC:DEC = 1:1 v/v)	61	545 mA h/g (100 mA/g) 367 mA h/g (5 A/g)	~92% @ 100 mA/g (after 100 cycles)	[130]
$SnSe_2$/RGO	Nanocomposites	1 M $NaClO_4$ (in EC:DMC = 1:1 v/v)	83	528 mA h/g (100 mA/g) 365 mA h/g (2 A/g)	87% @ 100 mA/g (after 100 cycles)	[135]
SnSe NSCs	Nanosheet clusters	1 M $NaPF_6$ + 5% (in DC:DEC = 1:1 v/v)	~95	~400 mA h/g (100 mA/g) 16 mA h/g (40 A/g)	28% @ 5 A/g (after 100 cycles)	[136]
$FeSe_2$	Microspheres	1 M $NaCF_3SO_3$ (in DEGDME)	~99	447 mA h/g (100 mA/g) 226 mA h/g (25 A/g)	89% @ 1 A/g (after 2,000 cycles)	[137]
$FeSe_2$@C	Nanorods	1 M $NaClO_4$ + 5% FEC (in PC)	63	568 mA h/g (100 mA/g) 245 mA h/g (10 A/g)	90% @ 10 A/g (after 3,000 cycles)	[138]
$FeSe_2$/GC	Microspheres	1 M $NaClO_4$ + 5% FEC (in EC:DC = 1:1 v/v)	58	540 mA h/g (200 mA/g) 417 mA h/g (5 A/g)	88% @ 200 mA/g (after 200 cycles)	[139]
$CoSe_2$	Urchin-like	1 M $NaCF_3SO_3$ (in DEGDME)	96	434 mA h/g (100 mA/g) 97 mA h/g (50 A/g)	98% @ 1 A/g (after 1,800 cycles)	[140]
CoSe@100CSs	Nanoparticles/carbon spheres	1 M $NaCF_3SO_3$ (in DEG:DME = 1:1 v/v)	99	900 mA h/g (100 mA/g) 535 mA h/g (2 A/g)	51% @ 4 A/g (after 10 000 cycles)	[141]
Sb2Se_3/rGO	Nanorods	1 M $NaCF_3SO_3$ (in DEGDME)	73	656 mA h/g (100 mA/g) 223 mA h/g (2 A/g)	98% @ 100 mA/g (after 50 cycles)	[142]
$MoSe_2$−NiSe−C	Microspheres	1 M $NaClO_4$ + 5% FEC (in EC:DMC = 1:1 v/v)	69	460 mA h/g (100 mA/g) 301 mA h/g (3 A/g)	well-maintained @ 0.5 A/g (after 80 cycles)	[134]
$MoSe_2$−NiSe	Microspheres	1 M $NaClO_4$ + 5% FEC (in EC:DMC = 1:1 v/v)	74	–	~66% @ 0.5 A/g (after 80 cycles)	[134]
$SnSe_{0.5}S_{0.5}$/C	Nanoparticles/microparticles	1 M $NaClO_4$ + 5% FEC (in EC:DEC = 1:1 v/v)	70	683 mA h/g (100 mA/g) 506 mA h/g (1 A/g)	~86% @ 200 mA/g (after 100 cycles)	[132]
$Ni_{0.85}Se$/C	Nanowires	1 M $NaClO_4$ + 5% FEC (in PC)	72	397 mA h/g (83.2 mA/g) 172 mA h/g (4.16 A/g)	97% @ 83.2 mA/g (after 100 cycles)	[143]
Cu−$CoSe_2$	Microboxes	1 M $NaClO_4$ + 5% FEC (in EC:DEC = 1:1 v/v)	65	492 mA h/g (50 mA/g) 185 mA h/g (3 A/g)	94% @ 1 A/g (after 500 cycles)	[133]
Fe_2CoSe_4	Nanoparticles	1 M $NaCF_3SO_3$ (in DEG:DME = 1:1 v/v)	87	816 mA h/g (50 mA/g) 400 mA h/g (32 A/g)	95% @ 1 A/g (after 100 cycles)	[131]

Table 4
Comparison of the electrochemical performances of MoS_2 and SnS_2 with different structures.

Materials	Morphology	Electrolytes	1st Coulombic efficiency (%)	2nd sodiation capacity (mA h/g)	Cycling retention	Ref.
MoS_2	Nanoflowers	1 M $NaCF_3SO_3$ (in DEGDME)	90.1	300 mAh/g (1 A/g) 195 mAh/g (10 A/g)	–	[72]
	Restacked microplates	1 M $NaCF_3SO_3$ (in DEGDME)	~72	~125 mAh/g (50 mA/g) ~50 mAh/g (1 A/g)	~40% @ 50 mA/g(after 70 cycles)	[74]
	Worm-like	1 M $NaPF_6$ (in FEC:DMC = 1:1 v/v)	~73	494 mAh/g (0.1 C)	83.1% @ 0.1 C (after 80 cycles)	[144]
	Ultrathin Nanosheets	1 M $NaClO_4$ (in EC:PC = 1:1 v/v)	40	510 mAh/g (40 mA/g) 320 mAh/g (320 mA/g)	72% @ 40 mA/g (after 100 cycles)	[75]
SnS_2	Nanosheets	1 M $NaClO_4$ (in EC:DEC = 1:1 v/v)	~55	540 mAh/g (200 mA/g)	~20% @ 200 mA/g (after 100 cycles)	[76]
	Bulk	1 M $NaClO_4$ (in EC:DEC = 1:1 v/v)	~73	~340 mAh/g (200 mA/g)	~15% @ 200 mAh/g (after 100 cycles)	[83]
	Nanosheets	1 M $NaClO_4$ + 5% FEC (in PC)	59	685 mAh/g (100 mA/g) 435 mAh/g (2 A/g)	88.2% @ 100 mA/g (after 50 cycles)	[85]
	Nanowall arrays	1 M $NaPF_6$ + 5% FEC (in EC:DEC:PC = 4:4:2 v/v)	75.3	730 mAh/g (100 mA/g) 474 mAh/g (5 A/g)	85% @ 500 mA/g (after 100 cycles)	[86]
	Nanoparticles	1 M $NaPF_6$ + 5% FEC (in EC:DEC:PC = 4:4:2 v/v)	75	~500 mAh/g (100 mA/g) ~100 mAh/g (5 A/g)	~75% @ 500 mA/g (after 100 cycles)	[86]
	Nanosheets on hierarchical tubular structures	1 M $NaClO_4$ (in EC:DEC = 1:1 v/v)	~36	652 mAh/g (50 mA/g) 299 mAh/g (500 mA/g)	58.5% @ 50 mA/g (after 50 cycles)	[145]

Recently, MXene coupled with other types of materials has drawn considerable attention [176–179] For example, MXene/SnS_2 shows remarkable electrochemical performance by combining their advantages: the metallic conductivity of MXene reduces the fading capacity of SnS_2, and the high capacity of SnS_2 provides numerous diffusion paths [178]. Zhao et al. prepared an alkali-induced 3D-crinkled porous Ti_3C_2 MXene coupled with NiCoP nanoparticles [176]; the bimetallic phosphide may have the richer redox reaction sites and stability as mentioned in the previous section. Herein, MXene functions as an electrical conductivity enhancer and elastic substrate to improve the charge transfer and alleviate the volume change. With this strategy, Ti_3C_2/NiCoP exhibits a capacity of 416.9 mA h/g at a current density of 0.1 A/g that significantly increases when compared with pure Ti_3C_2. As a result of the aforementioned synergetic effect, its cycling stability is also better than that of Ti_3C_2/Ni_2P. It is remarkable that the pseudocapacitance contribution of this material is extremely high; with a scan rate of only 0.3 mV/s, its contribution can reach 82.0%.

The electrochemical performances of the selected MXene anode materials for NIBs are summarized in Table 6. Overall, MXene may be considered a potential candidate for fast charge/discharge large-scale energy storage systems. However, the relatively lower capacity is an issue, which deserves more investigation and improvements in future studies.

2.5. Silicene, germanene, stanene, and borophene

Silicene, a 2D allotrope silicon with a hexagonal honeycomb structure similar to that of graphene [186] has been predicted to be an extraordinary 2D anode material. Compared to bulk Si, where the binding energy is +0.6 eV (unfavorable), silicene has a negative binding energy of −0.32 eV as Na is inserted; this implies that the Na storage can be achieved in silicene [39,40]. The energy barrier exhibits a reduction from 1.06 eV in bulk silicon to 0.14 eV in silicene that results in considerably faster diffusion rates [40]. The improvements in binding energetics as well as in Na diffusion rates suggest that silicene is a potential anode material for NIBs.

Germanene was first proposed in 2009 [187]. It is composed of a single layer of germanium atoms, which are individually deposited onto a substrate under specific conditions [188]. Germanium has atomic and electronic structures similar to silicon; accordingly, germanene (a 2D form of germanium) is expected to exhibit a high capacity for Li^+ and Na^+ batteries [189]. Bhuvaneswari et al. investigated the surface assimilation of Na/Na^+ on bare germanene and hydrogenated germanene nanosheets; the strong adsorption of Na^+ on both nanosheets suggests that they can be used as anode materials for NIBs.

Stanene is a 2D material composed of tin atoms arranged in a hexagonal layer. Similar to silicene and germanene, it is also a potential anode for batteries. On the other hand, a 2D sheet of boron (named borophene), synthesized on the surface of silver (111) [190], features a low atomic weight and metallic character, which make it an appealing option for the anode of NIBs. By using the study of first-principles, Zhang et al. found that the energy barrier in Na diffusion along the uncorrugated direction is better than that of graphene [191,192]. On the other hand, other calculations indicate that borophene can provide a super-high capacity of 1,218 mA h/g and preserve the metallic character and structural integrity at different sodium concentrations [41]. Overall, borophene is a potential anode material for NIBs.

The free-standing forms of these materials, however, remain inexistent in nature, where their intrinsic properties may be affected by the interactions between the deposited atomic layers and the substrates [26]. Shi et al. combined the heterostructure of silicene with graphene (Si/G); the latter served as a substrate and

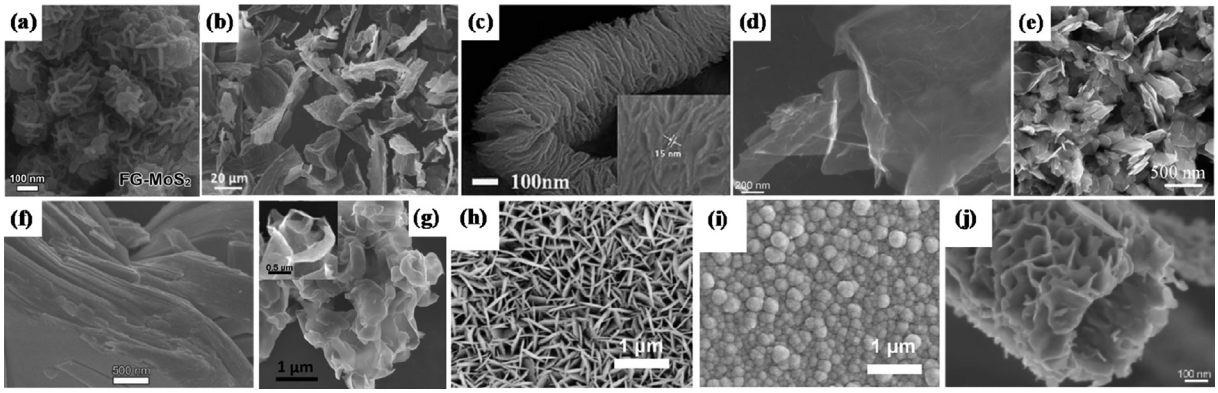

Fig. 5. SEM images of (a) MoS_2 nanoflowers [72] (reprinted with permission, copyright 2014, John Wiley and Sons), (b) MoS_2 restacked microplates [74] (reprinted with permission, copyright 2015, Elsevier), (c) worm-like MoS_2 [144] (reprinted with permission, copyright 2015, The Royal Society of Chemistry), (d) MoS_2 ultrathin nanosheets [75] (reprinted with permission, copyright 2015, John Wiley and Sons), (e) MoS_2 nanosheets [76] (reprinted with permission, copyright 2016, American Chemical Society), (f) bulk SnS_2 [83] (reprinted with permission, copyright 2015, The Royal Society of Chemistry), (g) SnS_2 nanosheets [85] (reprinted with permission, copyright 2015, American Chemical Society), (h) SnS_2 nanowall arrays [86] (reprinted with permission, copyright 2017, American Chemical Society), (i) SnS_2 nanoparticles [86] (reprinted with permission, copyright 2017, American Chemical Society), and (j) SnS_2 nanosheets on hierarchical tubular structures [145] (reprinted with permission, copyright 2018, Elsevier).

protective layer to preclude the contamination of silicene. Their computational results show that the Si/G heterostructure not only preserves silicene's large sodium capacity (487 mA h/g) but also provides low migration energy barriers for sodium [193]. The hydrogenated borophene (borophane, boron hydride, or hydrogen boride), fabricated by Nishino et al. [194], is not grown on a substrate. Through different analyses, calculations show that the hydrogenated borophene exhibits high electronic conductivity, stable structure, low charging voltage, and high capacity (1,133.8 mA h/g) as the intercalation of Na adatoms transpires [195].

3. *In situ* characterization techniques for 2D anodes in Na-ion batteries

Although 2D anode materials exhibit notable results in NIBs, its energy-storage mechanisms have not been well investigated. To understand the energy-storage mechanisms and explore the potential of 2D anode materials, various *in situ*/*operando* characterization techniques have been utilized. These include *in situ* X-ray diffraction (XRD), *in situ* Raman spectroscopy, *in situ* X-ray adsorption spectroscopy (XAS), *in situ* transmission electron microscopy (TEM), *in situ* transmission X-ray microscopy (TXM), and *in situ* atomic force microscopy (AFM). These techniques are employed to investigate structural and morphological evolutions, the interface change between electrode and electrolyte, and the dynamic process involved during charging/discharging [196–199].

3.1. *In situ/operando XRD*

The *in operando* XRD is an extremely powerful and a convenient technique to monitor the structural evolution and phase transformation of 2D anode materials during the NIB operation. It enables the realization of how anode materials interact with Na ions and why some of them undergo irreversible structural changes. The preparation of an *in operando* XRD cell is relatively simple. Typically, a battery cell with an X-ray window covered with a beryllium foil or Kapton tape is used, allowing X-rays to penetrate through the electrode materials and reach the detectors [199].

Two-dimensional materials are formed by layers of atomic slabs, which are connected by a weak van der Waals force; thus, Na ions can intercalate in or de-intercalate from a large slab spacing fast and reversibly [197]. Wang et al. utilized *in situ* XRD to detect the structural change of MoS_2 anode during cycling; two-phase structural transitions are observed in 1 V vs. Na^+/Na during the sodiation process (Fig. 9a) [61]. The phase changes from 2H–MoS_2 to 2H–$Na_{0.5}MoS_2$ in the first transition (0.85 V) and thereafter transfers to 1T–$NaMoS_2$ (0.75 V); the insertion of more Na ions (Na_xMoS_2,$1.0 < x < 1.5$) leads to no significant structural transition. The subsequent desodiation process initiates as a solid–solution reaction; thereafter, when 2.5 V is exceeded, a two-phase transition occurs from 1T–$Na_{0.5}MoS_2$ to 1T–MoS_2 (instead of 2H–MoS_2). This indicates that the structure of MoS_2 can be partially recovered at the end of the desodiation process when $x < 1.5$. The charge storage mechanism of the SnS_2@C hollow nanospheres was studied by Li et al. through *in situ* XRD and HRTEM [200]. The *in situ* XRD patterns show the continuous decrease in the main peaks of SnS_2 upon the initial sodiation process. Neither Na_2S nor Na_xSn, can be observed from the patterns possibly because of the low crystallinity; nevertheless, Na_2S and $Na_{15}Sn_4$ can still be observed from the HRTEM image at the full sodiation state, revealing the presence of alloying reaction. At a full desodiation state (3 V), SnS and SnS_2 can be detected, which indicates that the slow reaction kinetics results in the partially irreversible recovery of SnS_2 from Sn. Yang et al. performed *in situ* XRD on a NIB cell with chemically exfoliated V_5S_8 and graphite hybrid nanosheet (ce-V_5S_8–C) anode, as shown in Fig. 9b. The results reveal five stages during the sodiation/desodiation process: (I) the intercalation reaction (1.5–0.4 V); (II) the combination of intercalation and conversion reaction (0.4–0.25 V); (III) the conversion reaction (0.25–0.01 V); (IV) the dissociation reaction from Na_2S to Na ion, V, and $NaxV_5S_8$ (0.01–1.5 V); and (V) the deintercalation from $NaxV_5S_8$ to V_5S_8 nanosheets (1.5–3 V) [201]. The intercalation/deintercalation and conversion processes seem to be reversible, and the irreversible capacity results from the V residue, S dissolution, and SEI formation in the first cycle. Ou et al. published a series of *in situ* XRD studies on 2D anode materials including chemically exfoliated NbS_2 (ce-NbS_2) nanosheets [202], $NiSe_2$/rGO [203], $CoSe_2$ [204], and Sb_2Se_3 nanorod/rGO [142]. The result indicates that ce-NbS_2 nanosheets can remain in their crystal structure during Na ion intercalation/deintercalation; this leads to a long cycle life [202]. In the potential window between 0.4 and 3 V, $NiSe_2$/rGO and $CoSe_2$ anodes exhibit reversible intercalation and conversion reactions [203,204]. When the $CoSe_2$ anode is discharged below 0.4 V, however, a deep conversion reaction of CoSe occurs and forms Na_2Se and metallic Co; these result in pulverization and structural collapse. The Sb_2Se_3 nanorod/rGO anode material exhibits a high capacity (up to 682 mA h/g); as

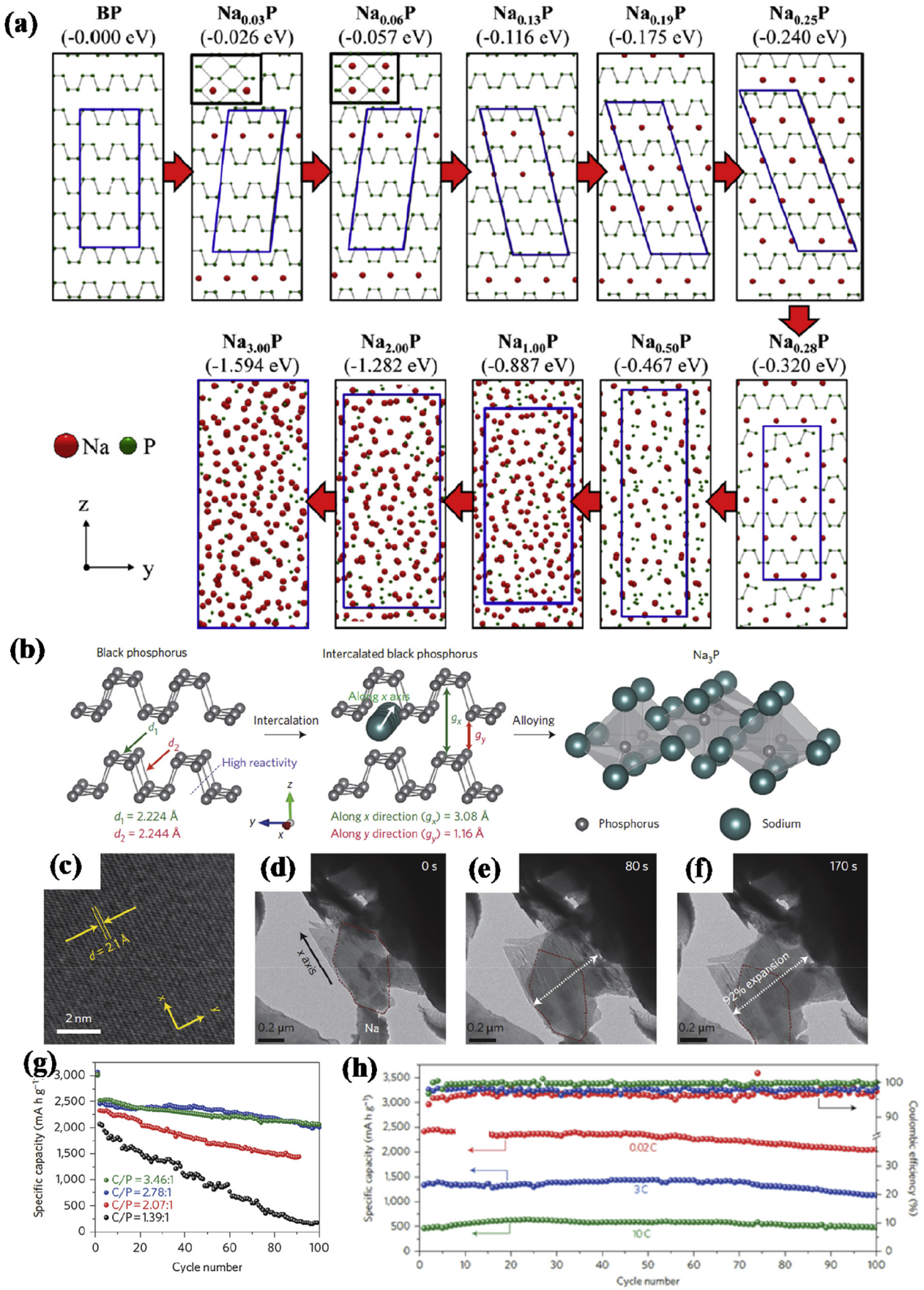

Fig. 6. (a) Sodiation mechanism of black phosphorous [153]. Reprinted with permission, copyright 2015, American Chemistry Society. (b) Illustration of sodiation of black phosphorous (BP) [38]. Reprinted with permission, copyright 2015, Springer Nature. (c) HRTEM image of BP. (d–f) Time-lapse TEM images of sodiation of BP [38]. Reprinted with permission, copyright 2015, Springer Nature. (g–h) Cycling stability of phosphorene–graphene anode [38]. Reprinted with permission, copyright 2015, Springer Nature.

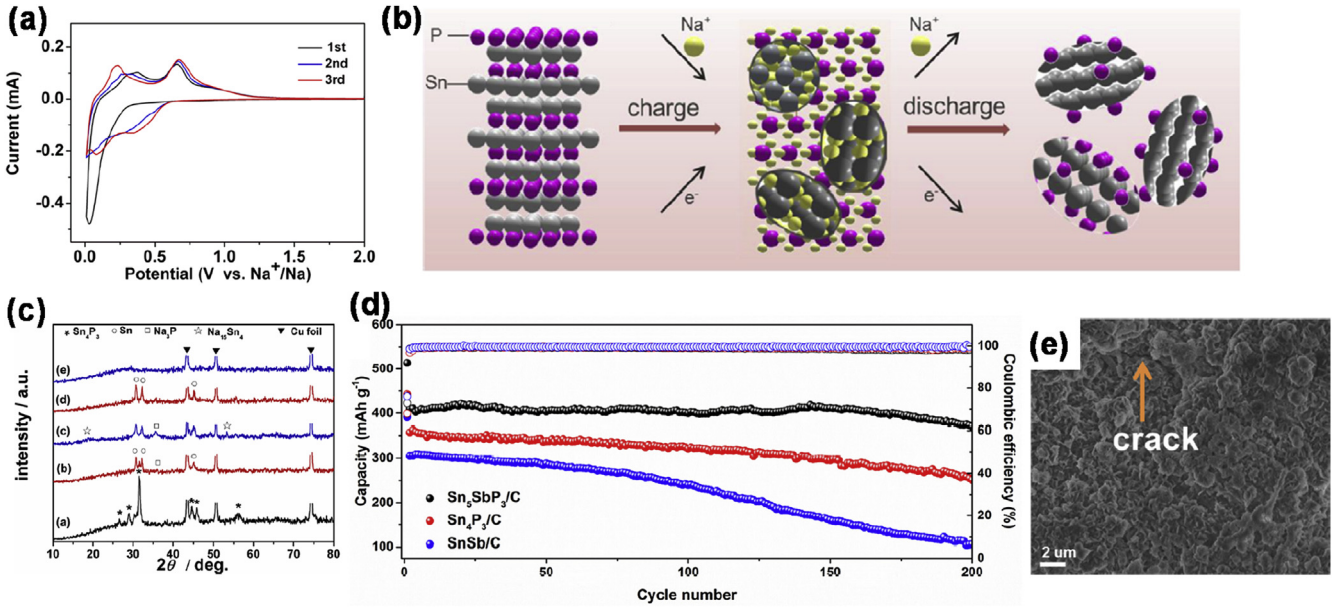

Fig. 7. (a) Illustration of sodiation/desodiation of Sn_4P_3 [166]. Reprinted with permission, copyright 2014, American Chemistry Society. (b) *Ex situ* XRD patterns of Sn_4P_3 at different voltages [166]. Reprinted with permission, copyright 2014, American Chemistry Society. (c) CV curves of Sn_4P_3 at a rate of 0.05 mV/s [166]. Reprinted with permission, copyright 2014, American Chemistry Society. (d) Cycling performance of Sn_5SbP_3/C, Sn_4P_3/C, and SnSb/C electrodes [167]. Reprinted with permission, copyright 2017, Elsevier. (e) SEM images of SnSb/C composite after 100 cycles at 1,000 mA/g [167]. Reprinted with permission, copyright 2017, Elsevier.

demonstrated by the *in situ* XRD, it combines the Na-ion intercalation, the conversion reaction between Na ion and Se, and the alloying reaction between Na ion and Sb (Fig. 9c) [142]. Ali et al. probed the phase transformation in a binary transition metal selenide electrode (Fe_2NiSe_4) during cycling as displayed in Fig. 9d; the reversible conversion reaction can be detected as follows [205].

$$Fe_2NiSe_4 + 8Na^+ + 8e^- \leftrightarrow 2Fe + Ni + 4Na_2Se \quad (1)$$

3.2. *In situ* Raman

In situ Raman spectroscopy can be utilized to detect the laser-induced vibrational, rotational, and other low-frequency transitional modes in anode materials [199]; therefore, the evolution of structural and electronic properties during sodiation/desodiation can be investigated. Apart from the foregoing, the crystal structural change in the amorphous anode material is difficult to detect by *in situ* XRD; on the other hand, *in situ* Raman spectroscopy is a power tool for probing the structural evolution. Xie et al. conducted *in situ* Raman spectroscopy to study the phase transition of MoS_2 nanosheets vertically aligned on a carbon paper (MoS_2@C) during battery cycling, as shown in Fig. 10 [206]. The reversible phase transition from 2H—MoS_2 (379 and 405 cm^{-1}) to 1T-MoS_2 (156, 218, and 327 cm^{-1}) and 1T—Na_yMoS_2 is detected during the Na-ion intercalation/deintercalation process. When the cell is discharged from 0.2 to 0.1 V, the peaks of 1T—Na_yMoS_2 decrease; this indicates the decomposition of 1T—Na_yMoS_2 into Mo and Na_yS. During the discharge process, the blue-shift of the D-band and the red-shift of the G-band can be probed, suggesting that Na ions are intercalated into the carbon material. Lane et al., on the other hand, recorded the *in situ* Raman spectrum of metallic 1T—MoS_2 anodes; the two main peaks at 150 cm^{-1} (J_1) and 220 cm^{-1} (J_2) remain without the formation of other peaks, revealing that the phase of 1T—MoS_2 is unchanged [207]. Chao et al. utilized *in situ* Raman to investigate the self-branched SnS_2 (B—SnS_2) anode; the result indicates that the B—SnS_2 anode undergoes good reversibility during intercalation, conversion, and alloying reactions even at a high charge/discharge rate (at 5 A/g) [124].

3.3. *In situ* TEM

In situ TEM has been considered as a powerful technique to observe the microstructural transformation and ion diffusion directly at the atomic scale during sodiation and desodiation processes. The electrochemical reactions between the electrode materials and electrolyte can be detected by lattice image alternations, selected area electron diffraction, electron energy loss spectroscopy, and energy-dispersive X-ray spectroscopy [196].

Sun et al. prepared a phosphorene/graphene hybrid anode; it exhibits a high specific capacity of 2,440 mA h/g at a current density of 50 mA/g with an excellent cycling retention (83%) after 100 cycles [38]. The sodiation mechanism is studied through *in situ* TEM; the results show a 92% volume expansion along the y-axis of the phosphorene layers, but no significant change is observed along the x-axis, as shown in Fig. 4c—f. This indicates that the Na ions preferentially intercalated along the x-axis of phosphorene layers and formed a Na_3P alloy. The graphene layers in the hybrid material acted as an electrical network and elastic buffer to accommodate the expansion of phosphorene layers; this led to good cycling stability. Kim et al. also utilized *in situ* TEM to investigate the sodiation mechanism in single-crystalline BP flakes [208]. The setup of the TEM holder is shown in Fig. 11a. The BP was on the TEM grid, and a Na metal was used as the counter electrode with surface-coated Na_2O solid electrolyte. The Na ions initially intercalated in the same layered channels and then diffused toward the selective zigzag intercalation channels. Gao et al. directly tracked the migration of Na ions in layered SnS_2 nanostructures at the atomic scale by the *in situ* TEM technique, as displayed in Fig. 11b [209]. During the sodiation process, SnS_2 transformed to a highly defective and expanded Na_xSnS_2 through a two-phase reaction. In the desodiation process, it underwent a solid-solution reaction with the formation of nano-sized intermediate $Na_{0.5}SnS_2$ with row-ordering within every (001) Na planes. The observation of asymmetric sodium insertion and extraction pathways provides valuable insights into the origins of voltage hysteresis in NIBs. Gao's group also studied the Na-ion storage mechanism of MoS_2 nanosheets. The sodiation process proceeded *via* a two-phase reaction, which

Table 5
Electrochemical performance of selected phosphorene and metal phosphide anode materials for Na-ion batteries.

Materials	Morphology	Electrolytes	1st Coulombic efficiency (%)	2nd sodiation capacity (mA h/g)	Cycling retention	Ref.
Phosphorene/graphene	Nanosheets	1 M $NaPF_6$ + 10% FEC (in EC/DEC)	~80	85% @ 50 mA/g (after 100 cycles)	83% @ 50 mA/g (after 100 cycles)	[38]
Few-layer phosphorene	Nanosheets	1 M $NaClO_4$ + 5% FEC (in PC)	~51	1,878.4 mA h/g (100 mA/g) 321 mA h/g (2.5 A/g)	61% @ 100 mA/g (after 50 cycles)	[168]
Sn_4P_3/C	Agglomerated nanoparticles	1 M $NaPF_6$ + 5% FEC (in EC/DEC)	77	816 mA h/g (50 mA/g) 349 mA h/g (1,000 mA/g)	86% @ 100 mA/g (after 150 cycles)	[166]
Sn_4P_3	Microparticles	1 M $NaClO_4$ + 5% FEC (in EC:DEC = 1:1 v/v)	~82	718 mA h/g (100 mA/g)	92% @ 100 mA/g (after 100 cycles)	[25]
SnP_3/C	Nanoparticles	1 M $NaClO_4$ (in FEC:DMC = 1:1 v/v)	71	860 mA h/g (80 mA/g) 570 mA h/g (2,560 mA/g)	~99% @ 150 mA/g (after 150 cycles)	[159]
Sn_4P_3/MWCNTs	Nanotubes	1 M $NaClO_4$ (in FEC:DMC = 1:1 v/v)	72	520 mA h/g (100 mA/g) 259 mA h/g (1 A/g)	90% @ 100 mA/g (after 120 cycles)	[160]
Sn_4P_3/RGO (10.4 wt% C)	Nanoparticles/nanosheets	1 M $NaClO_4$ + 5% FEC (in PC)	46	670 mA h/g (100 mA/g) 391 mA h/g (2 A/g)	~74% @ 1 A/g (after 1,500 cycles)	[40]
$Ni_2P \subset pGN$	Yolk−shell nanoparticles	1 M $NaCF_3SO_3$ (in DEGDME)	52	211 mA h/g (100 mA/g) 101 mA h/g (2 A/g)	89% @ 200 mA/g (after 100 cycles)	[161]
Sn_5SbP_3/C	Microparticles	1 M $NaClO_4$ + 5% FEC (in PC)	~74	~454 mA h/g (100 mA/g) 352 mA h/g (2 A/g)	95% @ 500 mA/g (after 200 cycles)	[167]
CoP@C-RGO−NF	Polyhedral	1 M $NaClO_4$ + 5% FEC (in PC)	47	713 mA h/g (100 mA/g) 155 mA h/g (1.6 A/g)	51% @ 100 mA/g (after 100 cycles)	[162]
CoP	Nanoparticles	1 M $NaClO_4$ (in EC:DEC = 1:1 v/v)	65.2	570 mA h/g (100 mA/g) 80 mA h/g (2 A/g)	70% @ 100 mA/g (after 25 cycles)	[163]
FeP	Nanoparticles	1 M $NaClO_4$ (in EC:DEC = 1:1 v/v)	~62	420 mA h/g (50 mA/g) 60 mA h/g (500 mA/g)	69% @ 100 mA/g (after 60 cycles)	[165]
H−FeP@C@GR	Nanocomposites	1 M $NaClO_4$ (in FEC:PC = 1:1 v/v)	66	620 mA h/g (100 mA/g) 237 mA h/g (1.6 A/g)	~54% @ 100 mA/g (after 250 cycles)	[164]
NCP@FCNT−FS	Freestanding films	1 M $NaClO_4$ + 5% FEC (in PC)	~56	500 mA h/g (500 mA/g) 276 mA h/g (8 A/g)	~33% @ 500 mA/g (after 100 cycles)	[169]

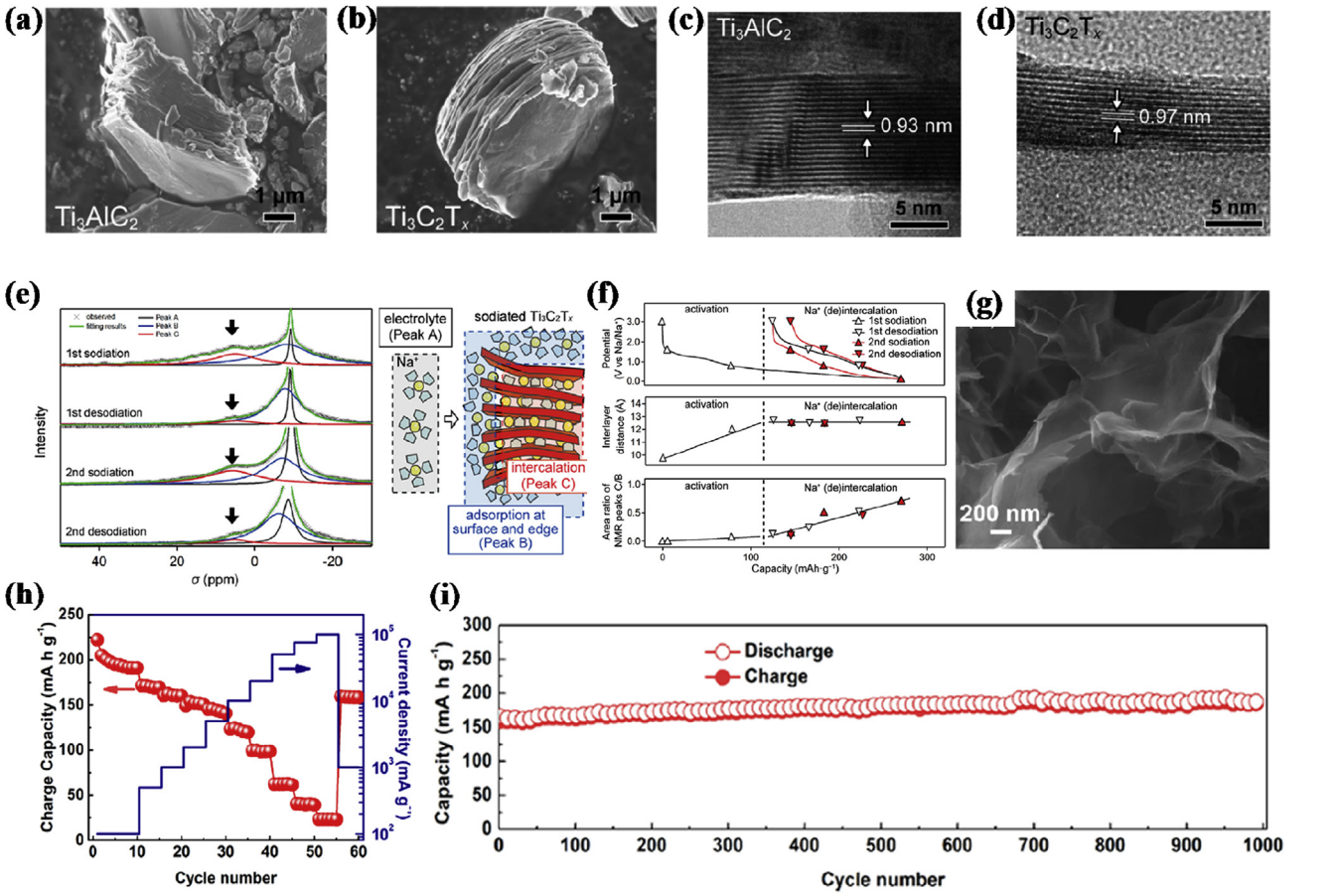

Fig. 8. (a–d) SEM and TEM images of Ti_3AlC_2 and Ti_3C_2 [36]. Reprinted with permission, copyright 2016, American Chemistry Society. (e) ^{23}Na MAS NMR spectra to identify the $Ti_3C_2T_x$ mechanism [36]. Reprinted with permission, copyright 2016, American Chemistry Society. (f) Change in interlayer distance and intercalated Na amount during two initial cycles [36]. Reprinted with permission, copyright 2016, American Chemistry Society. (g) SEM image of porous $Ti_3C_2T_x$ [37]. Reprinted with permission, copyright 2018, Elsevier. (h) Rate performance of porous $Ti_3C_2T_x$ [37]. Reprinted with permission, copyright 2018, Elsevier. (i) Long cycling performance of porous $Ti_3C_2T_x$ for 1,000 cycles at a current density of 1 A/g [37]. Reprinted with permission, copyright 2018, Elsevier.

started with the nucleation of a new phase of $NaMoS_2$; thereafter, the phase boundary diffused [210]. Zhang et al. also used *in situ* TEM to characterize the phase transformation of MoS_2 during cycling. In the sodiation process, the pristine 2H—MoS_2 nanosheets convert to 1T—$NaMoS_2$ in the first stage; they are thereafter transformed to Na_2S [211]. The microstructure evolution of MoS_2 nanosheets occurs during the sodiation and desodiation processes; the Na ions are easily extracted from the edge of the MoS_2 layer. This indicates that Na ions preferentially migrate along the edge of MoS_2 nanosheets and migrate smoothly in between MoS_2 layers. Using *in situ* TEM, Yao et al. investigated the sodiation kinetics and structural evolution in carbon-coated Sb_2S_3 nanorod electrodes, which are stacked by weak van der Waals forces [212]. The Na^+ ion intercalation and conversion/alloying reactions are observed (Fig. 11c); during the first sodiation process, the Na ions quickly intercalate into the voids of Sb_2S_3 at 146 nm/s, resulting in the amorphization of the Sb_2S_3 crystalline and a small volume expansion of approximately 54%.

3.4. *In situ AFM*

The *in situ* AFM technique, which is based on the indentation of a tip-shaped cantilever, can be utilized to probe the surface topography evolution by scanning the interface between the electrode and liquid electrolyte during battery cycling [199]. The SEI layer formation on the electrode surface in different electrolytes and at different potentials can be observed by the *in situ* AFM technique. It can also detect the real-time mechanical properties and the structural changes of electrode materials during the sodiation and desodiation processes. Lacey et al. assembled a microscale battery, which consisted of mechanically exfoliated MoS_2 flakes with copper connections and Na metal reference [213]. They utilized the *in situ* AFM method to analyze the sodium intercalation model of MoS_2 anode by a special cell design in a dry room environment, as shown in Fig. 12. After discharging to 0.4 V in the first sodiation process, a permanent structural wrinkling of the sodiated MoS_2 flakes is observed. The SEI layer immediately forms on both flake edges and planes before the sodiation process; the SEI thickness (20.4 ± 10.9 nm) is estimated through AFM analysis.

3.5. *In situ XAS*

The *in situ* synchrotron XAS is a powerful technique to detect the changes in the chemistry and bonding environment of 2D electrode materials during sodiation and desodiation processes [199]. The X-ray absorption near-edge structure (XANES) method can provide the oxidation states with the site-symmetry information. On the other hand, the extended X-ray absorption fine structure (EXAFS) method can deliver the local structural evolution in real time.

Bak et al. synthesized a 2D vanadium carbide MXene containing surface functional groups (V_2CT_x, T_x) and studied the charge storage mechanism of the V_2CT_x electrode by *in situ* synchrotron XANES, as

Table 6
Electrochemical performance of selected MXene anode materials for Na-ion batteries.

Materials	Morphology	Electrolytes	1st Coulombic efficiency (%)	2nd sodiation capacity (mA h/g)	Cycling retention	Ref.
Ti_3C_2 MXene/CNT-SA	Porous composite paper	1 M $NaClO_4$ + 5% FEC (in EC/PC = 1:1 v/v)	36	421 mA h/g (20 mA/g) 89 mA h/g (5A/g)	~132% @ 100 mA/g (after 500 cycles)	[37]
Ti_3C_2Tx	Layered structure	1 M $NaPF_6$ (in EC:PC = 1:1 v/v)	~54	~120 mA h/g (20 mA/g) ~70 mA h/g (500 mA/g)	~67% @ 20 mA/g (after 100 cycles)	[36]
a-Ti_3C_2 MNRs	Flat nanoribbons	$NaCF_3SO_3$ (in DME)	55	167 mA h/g (20 mA/g) 85 mA h/g (300 mA/g)	~86% @ 50 mA/g (after 200 cycles)	[180]
Ti_3C_2Tx	3D macroporous films	1 M $NaClO_4$ + 5%FEC (in EC:PC = 1:1 v/v)	~49	330 mA h/g (~88 mA/g) 120 mA h/g (8.8 A/g)	54% @ 880 mA/g (after 1,000 cycles)	[181]
V_2CTx	Lamellar structure	1 M $NaPF_6$ (in EC:DMC = 3:7 v/v)	53	90 mA h/g (10 mA/g) 50 mA h/g (1 A/g)	~68% @ 20 mA/g (after 100 cycles)	[182]
Ti_3C_2Tx/SnS_2 (5:1)	Flakes/nanoplates	1 M $NaClO_4$ + 5%FEC (in EC:PC = 1:1 v/v)	52	901 mA h/g (50 mA/g) 78 mA h/g (2 A/g)	~70% @ 100 mA/g (after 125 cycles, 0 °C)	[178]
BPQD/TNS	Black phosphorus quantum dots/nanosheets	1 M $NaClO_4$ + 5%FEC (in PC)	~33	~140 mA h/g (100 mA/g) ~100 mA h/g (2 A/g)	99% @ 1 A/g (after 1,000 cycles)	[179]
p-Ti_3C_2Tx	Porous structure	1 M $NaClO_4$ + 5%FEC (in EC:PC = 1:1 v/v)	30	~166 mA h/g (1 A/g) ~24 mA h/g (100 A/g)	113% @ 1 A/g (after 1,000 cycles)	[183]
Ti_3C_2/NiCoP	3D network/nanoparticles	1 M $NaClO_4$ + 5%FEC (in EC:DMC:EMC = 1:1:1 v/v)	69	~187 mA h/g (100 mA/g) ~103 mA h/g (2 A/g)	~59% @ 1 A/g (after 2,000 cycles)	[176]
Sulfur-decorated Ti_3C_2	Layered structure (coarse surface)	1 M $NaClO_4$ (in EC:PC = 1:1 v/v)	45	~211 mA h/g (400 mA/g) ~137 mA h/g (5 A/g)	~67% @ 2 A/g (after 1,000 cycles)	[177]
c-Ti_3C_2Tx	Foam-like porous structure	1 M $NaClO_4$ + 5%FEC (in EC:PC = 1:1 v/v)	~25	~240 mA h/g (20 mA/g) ~120 mA h/g (500 mA/g)	~98% @ 20 mA/g (after 50 cycles)	[184]
Ti_3C_2X	Multilayer-stacked nanosheets	1 M $NaClO_4$ (in EC:DEC = 4:6 v/v)	~88	~250 mA h/g (50 mA/g) ~90 mA h/g (800 mA/g)	85% @ 200 mA/g (after 1,000 cycles)	[185]

shown in Fig. 13a–b [182]. The V K-edge XANES result in the figure shows a reversible edge shift during the sodiation and desodiation processes; this indicates that the oxidation state change of vanadium is reversible. It demonstrates that the charge storage of the V_2CT_x anode in NIB may be mainly contributed by the redox reaction of vanadium (~0.2 electron transfer per vanadium) accompanied by Na-ion intercalation/deintercalation. Ma et al. characterized the charge storage mechanism of SnS_2–rGO electrodes through *in situ* Sn K-edge EXAFS spectra analysis [214]. The gap between Sn and Sn interaction changes, which implies that Na–Sn alloy phases form during the sodiation process (Fig. 13c). This result indicates that the SnS_2–rGO anode involves both conversion and alloying reactions.

3.6. *In situ* TXM

Various advanced X-ray imaging characterization methods, such as transmission X-ray microscopy (TXM), scanning transmission X-ray microscopy (STXM), scanning photoelectron microscopy, micro-X-ray fluorescence spectroscopy, and synchrotron radiation X-ray tomographic microscopy, have been established to investigate the charge storage mechanism of NIBs [199]. The strong power and nondestructive nature of X-ray enable it to penetrate through electrodes during battery operation. The wavelength of a probing X-ray beam ranges from nanometers to a few angstroms. Imaging with X-ray not only provides the morphological development of electrode materials but also detects the elemental and valence mapping information. The 3D X-ray tomography technique can provide the multidimensional information of electrode material at the μm–nm spatial resolution. Although *in situ* TEM is a powerful method to probe microstructural information and kinetic mechanism, its use is limited to thin samples (nanometer size). AFM can also provide microstructural information; however, it is restricted to surface analysis. The TXM instruments are usually operated with synchrotron sources; thus, they can probe large and thick samples with a broad area. Coin cells for *in operando* TXM measurement can therefore be utilized directly.

Wang et al. conducted *in operando* 2D TXM, XANES, and 3D tomography to obtain spatially resolved maps of phase transition and structural evolution as well as to analyze the electrochemically irreversible feature and large voltage hysteresis of the FeS anode in NIBs during the sodiation–desodiation process, as shown in Fig. 14 [215]. Based on the results, the FeS electrode undergoes conversion reaction during the first sodiation process. The phase transformation along with volume expansion occurs at the surface of particles in the initial sodiation stage; thereafter, the phase transformation propagates to the core until the particle is completely transformed to the Fe phase. During the desodiation process, the majority of the particles are transformed back to the FeS phase, and the volume contracts; however, some of the regions in the core remain in the Fe phase. It demonstrates that some of the Na ions are trapped in the center of particles; this results in the irreversible capacity in the initial cycle. The good reversibility of the FeS electrode is obtained after the second cycle; it reveals that the size reduction that resulted from particle fracture during the first cycle reduces the interfacial resistance and ion diffusion barriers. These results provide valuable insights for researchers to design a suitable morphology for FeS particles to achieve high-performance NIBs.

In addition to the aforementioned method, *in situ* neutron diffraction and *in situ* Fourier-transform infrared spectroscopy (FTIR) are also powerful techniques for the investigation of NIBs. The *in situ* neutron diffraction is usually applied to understand the ion transport mechanism during the sodiation/desodiation process [216]. Besides, FTIR can be utilized to understand the binding change during the charge/discharge process [217]. However, these

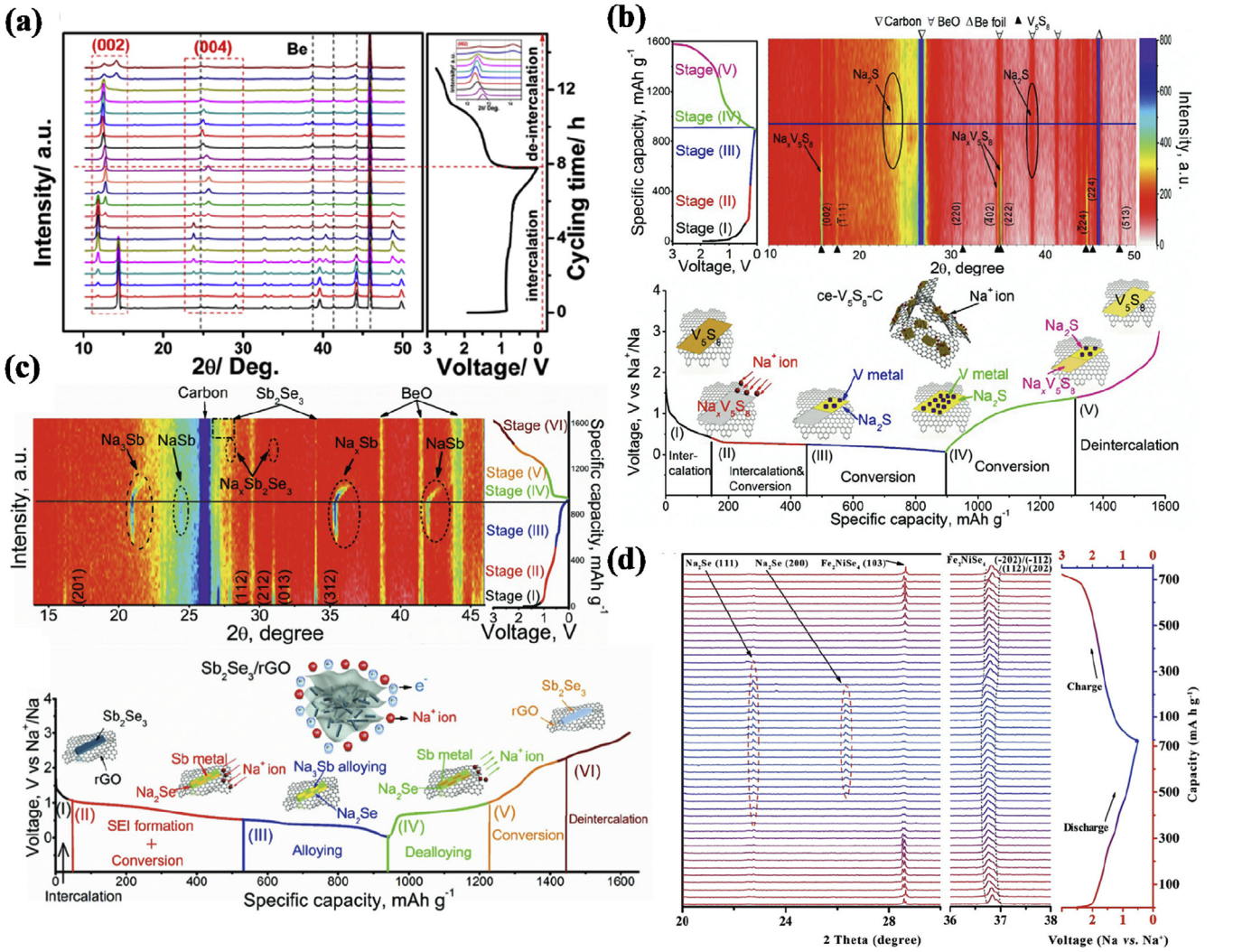

Fig. 9. (a) *In situ* XRD patterns of commercial MoS_2 containing different contents of electrochemically intercalated Na ions; inset of potential profile is for selected XRD patterns during Na deintercalation [61]. Reprinted with permission, copyright 2014, American Chemical Society. (b) Charge–discharge profiles, selected 2θ-region plot of *in situ* XRD results at different discharge/charge states of ce-V_5S_8–C hybrid anodes and schematic of energy storage mechanism of ce-V_5S_8–C hybrid anode at different stages [201]. Reprinted with permission, copyright 2017, The Royal Society of Chemistry. (c) *In situ* XRD patterns of the Sb_2Se_3/rGO anode operated at different states of charge vs. voltage during initial cycle and schematic of reaction mechanism of the Sb_2Se_3/rGO hybrid during charge/discharge process [142]. Reprinted with permission, copyright 2017, John Wiley and Sons. (d) *In situ* XRD analysis of Fe_2NiSe_4 electrode along with discharge and charge curves at a 100 mA/g scan rate [205]. Reprinted with permission, copyright 2014, John Wiley and Sons.

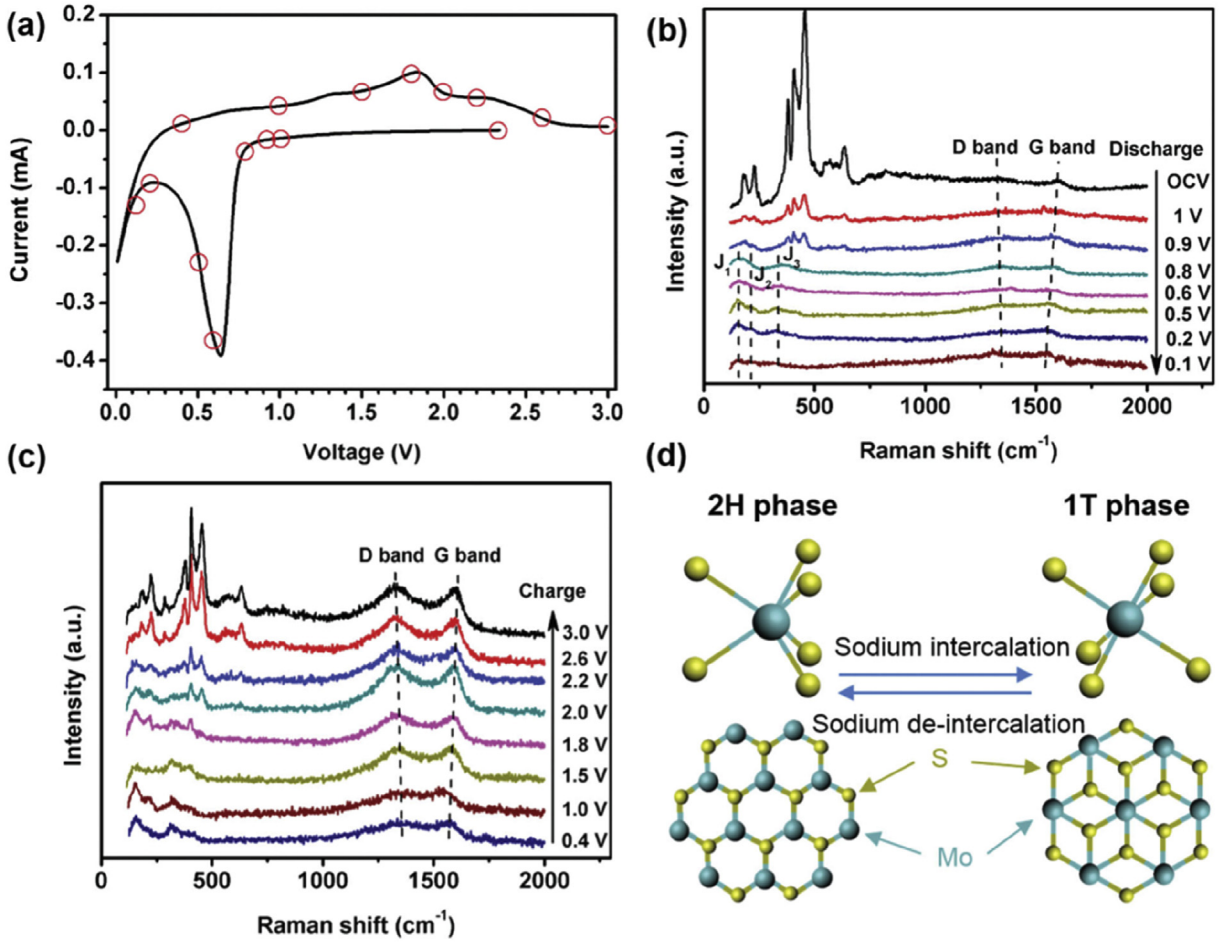

Fig. 10. (a) CV curve of the as-prepared MoS_2@C anode for sodium-ion batteries. *In situ* Raman spectra of the MoS_2@C electrode at different cut-off voltages during (b) discharge and (c) charge processes. (d) Schematic of phase transition between 2H−MoS_2 and 1T−MoS_2 during sodium intercalation/deintercalation [206]. Reprinted with permission, copyright 2016, John Wiley and Sons.

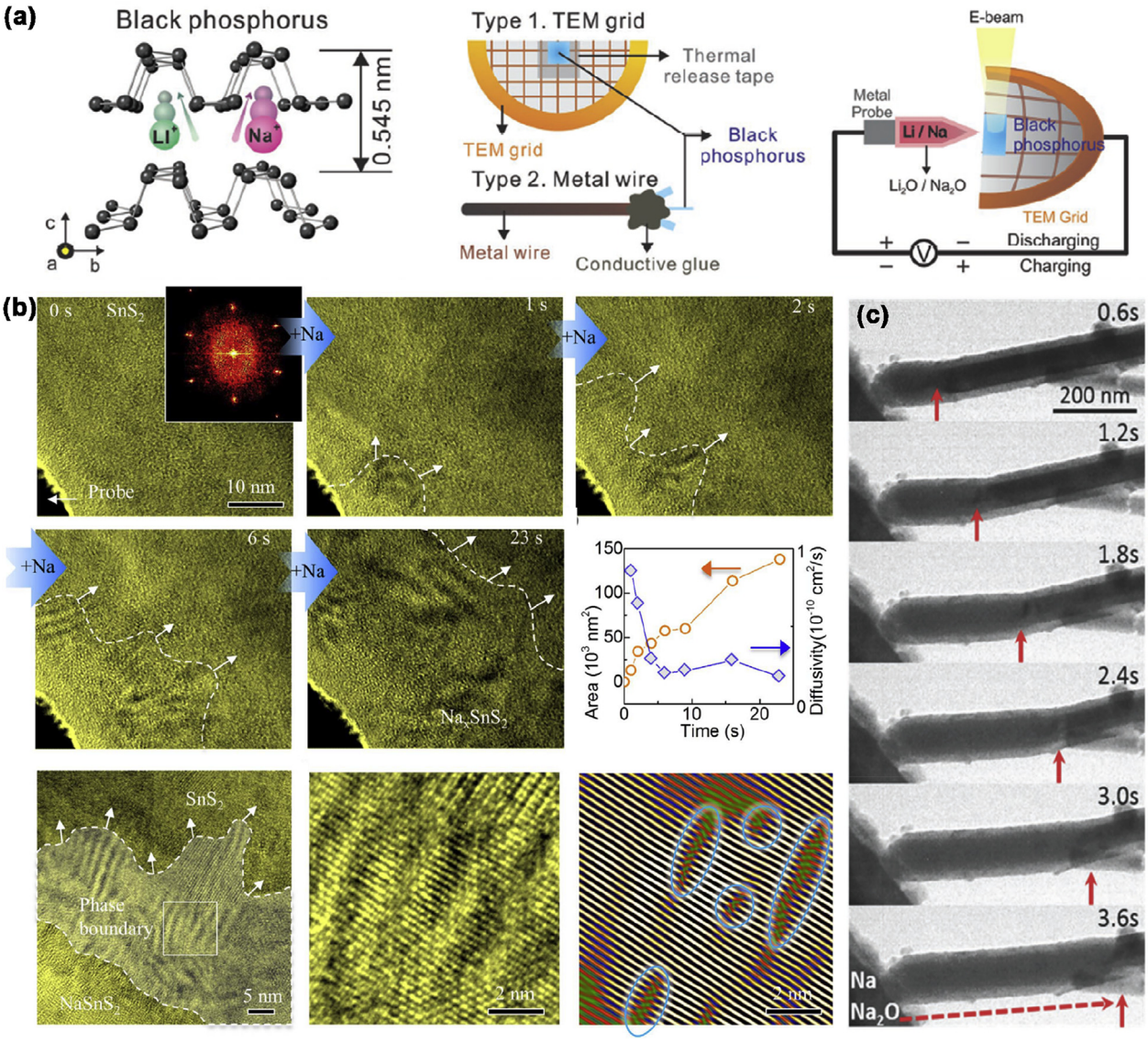

Fig. 11. (a) Schematics of sample preparation and *in situ* TEM setup for black phosphorus [208]. Reprinted with permission, copyright 2019, John Wiley and Sons. (b) High-resolution TEM tracking sodium insertion in SnS_2 in real-time [209]. Reprinted with permission, copyright 2017, Elsevier. (c) Morphological evolution of carbon-coated van der Waals-stacked Sb_2S_3 nanorod electrodes probed by *in situ* TEM [212]. Reprinted with permission, copyright 2017, John Wiley and Sons.

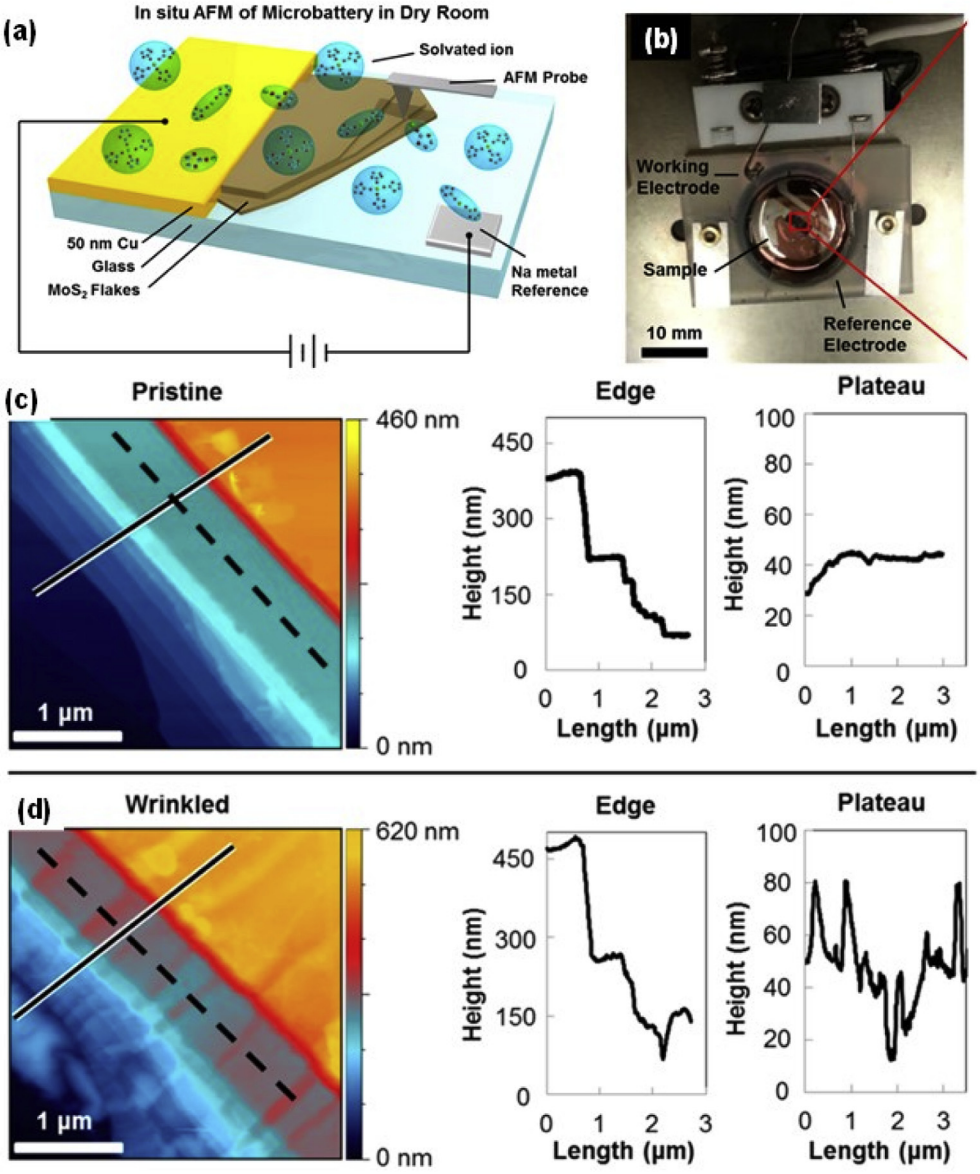

Fig. 12. (a) Schematic of planar microscale battery analyzed by AFM in liquid electrolyte and dry room environment for *in situ* measurements. (b) Digital image of planar Na/MoS_2 flake microscale battery within liquid electrochemical cell, which is used to conduct *in situ* measurements. *In situ* AFM images and line profiles (c) before and (d) after passivation of Na/MoS_2 planar microbattery from OCV to 0.4 V case [213]. Reprinted with permission, copyright 2015, American Chemical Society.

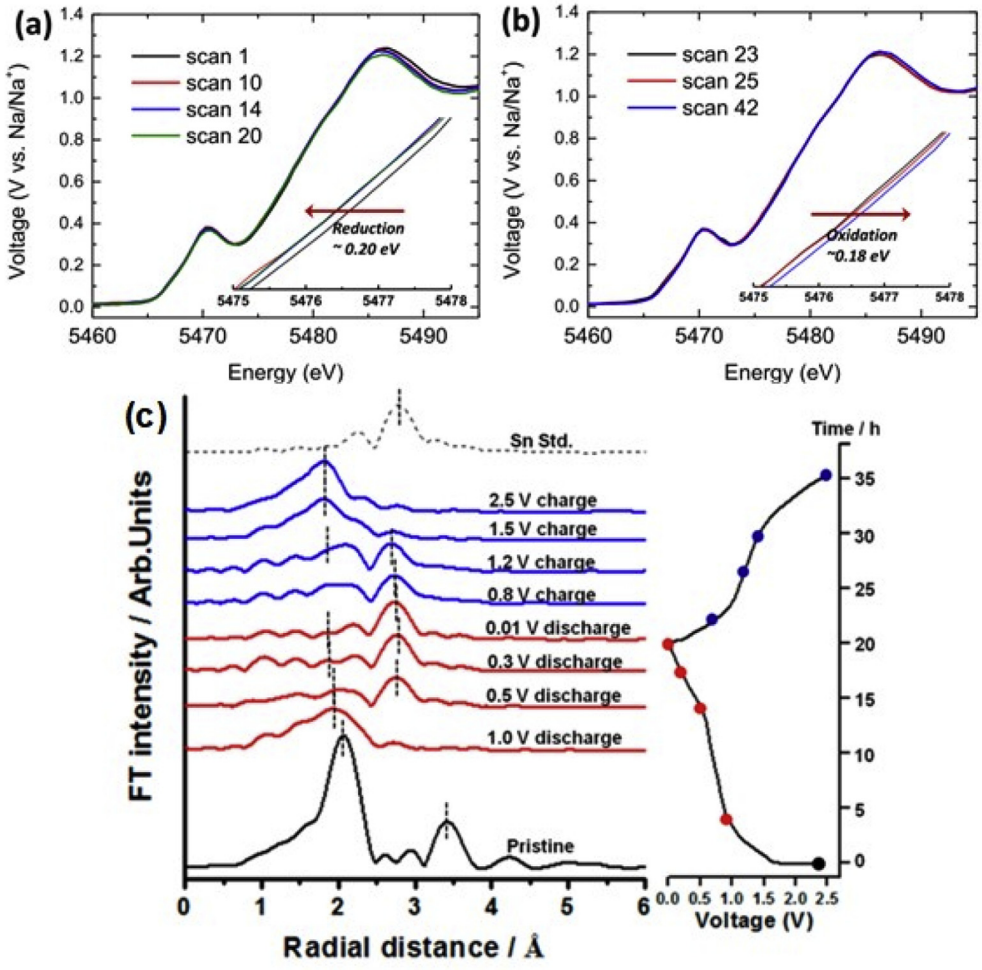

Fig. 13. *In situ* V K-edge XANES spectra of the V_2CT_x electrode during (a) sodiation and (b) desodiation processes [182]. Reprinted with permission, copyright 2017, John Wiley and Sons. (c) Sn K-edge EXAFS spectra of SnS_2–rGO electrodes at different voltages in the first cycle [214]. Reprinted with permission, copyright 2015, American Chemical Society.

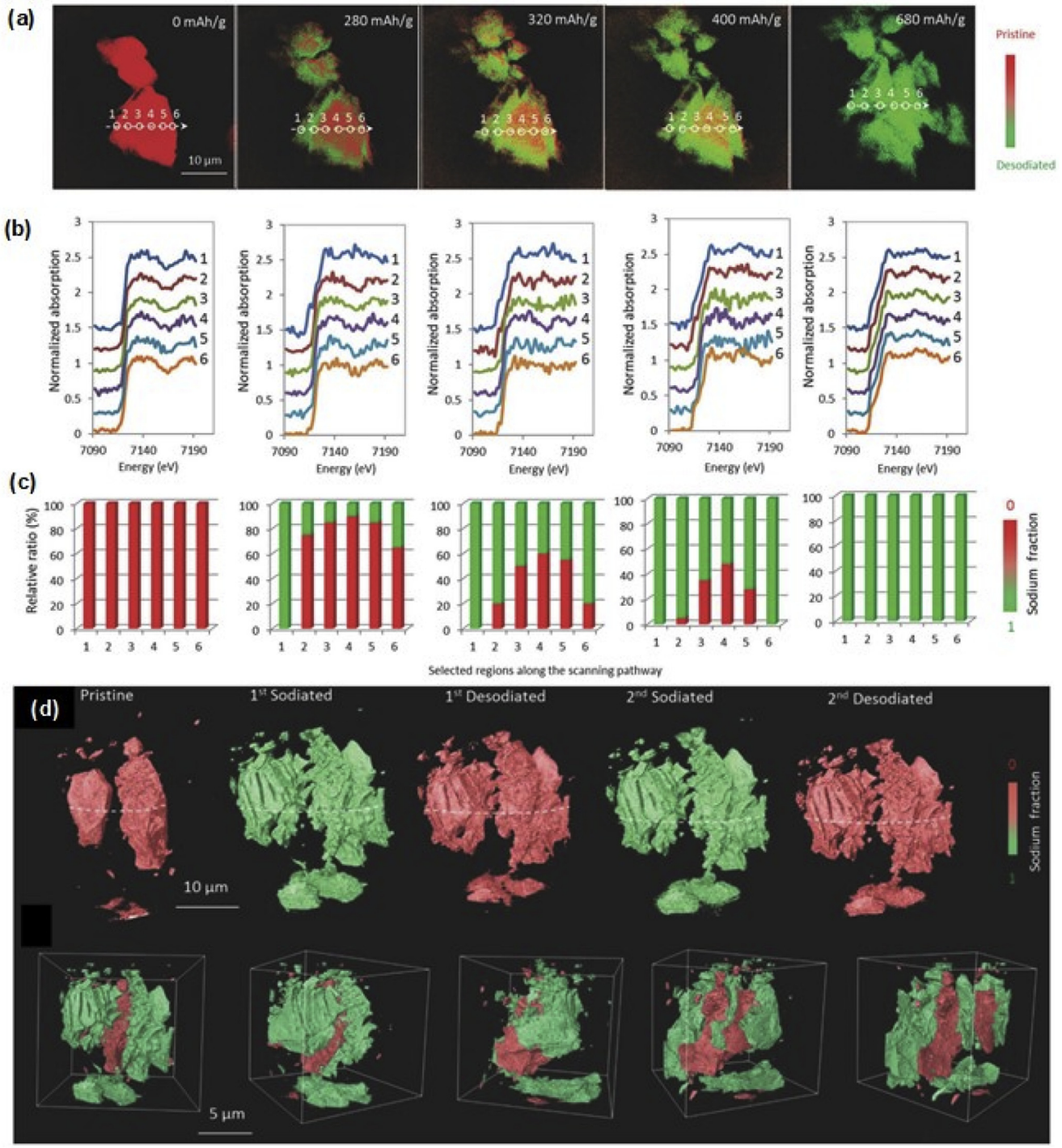

Fig. 14. (a)–(c) Phase composition analysis of selected states during the first sodiation cycle in Na–FeS batteries; (d) 3D tomography images of FeS during the first two cycles [199]. Reprinted with permission, copyright 2017, American Chemical Society.

techniques have not been reported in the field of 2D material-based NIBs so far.

4. Conclusion and prospects

This article reviews recent developments of 2D-layered materials in NIBs, including graphene and its derivatives, transition metal sulfides/selenides, phosphorene/metal phosphides, transition metal carbides/nitrides (MXene), and other graphene-like elemental analogs (silicene, germanene, stanene, and borophene). These 2D anode materials exhibit excellent electrochemical performances in NIBs because of their shortened paths for Na-ion diffusion and large surface areas for Na-ion absorption. Some of the 2D materials even provide high electronic conductivity, which enables considerable rate capability, such as transition metal selenides. A comprehensive review of various *in situ* characterization techniques to investigate the sodium storage mechanism of these 2D anode materials is also presented. It is anticipated that the higher performance 2D anode materials could be achieved in the future with better understanding of the charge storage mechanism using *in situ* electrochemical characterization methods.

The main sodiation/desodiation mechanism of graphene and MXene is intercalation which leads to low capacities but good cycle stabilities. As for transition metal sulfides/selenides and phosphorene/metal phosphides, the sodiation/desodiation mechanisms are usually combined with intercalation, conversion, and alloying. Conversion and alloying reactions would cause severe stacking and agglomeration after sodiation/desodiation processes. Thus, for these reasons, nanostructured designs and mixing with flexible carbons to minimize the stacking and agglomeration phenomena are the most common ways to achieve a better performance. There are still some challenges to the development of 2D materials. One of these is that 2D materials as anodes in NIBs usually have high reaction potential which results in low energy density. Another challenge is the complicated preparation method of 2D materials. For example, highly corrosive HF or the precursor of forming HF is usually used to synthesize MXene, which increases the safety risks.

Moreover, from the above challenges, 2D materials are still considered as the potential anode materials for NIBs. Recently, many more binary metal sulfides, selenides, and phosphides are under investigated owing to their synergistic effect. By mixing two or more metal ions, the self-agglomeration can also be reduced. Another potential application is to build a fast charging/discharging device because of the pseudocapacitive effect in some of the 2D materials. However, more investigations are needed in the future in this field.

Declaration of competing interest

The authors declare that they have no known competing financial interests or personal relationships that could have appeared to influence the work reported in this paper.

Acknowledgements

This work was financially supported by the Young Scholar Fellowship Program by the Ministry of Science and Technology (MOST) in Taiwan, under Grant MOST108-2636-E-007-007.

References

[1] P. Sehrawat, C. Julien, S.S. Islam, Mater. Sci. Eng. B 213 (2016) 12–40.
[2] B. Scrosati, J. Hassoun, Y.-K. Sun, Energy Environ. Sci. 4 (2011) 3287–3295.
[3] N. Nitta, F. Wu, J.T. Lee, G. Yushin, Mater. Today 18 (2015) 252–264.
[4] J.M. Tarascon, M. Armand, Nature 414 (2001) 359.
[5] N. Yabuuchi, K. Kubota, M. Dahbi, S. Komaba, Chem. Rev. 114 (2014) 11636–11682.
[6] H. Wang, S. Hamanaka, T. Yokoyama, H. Yoshikawa, K. Awaga, Chem. Asian J. 6 (2011) 1074–1079.
[7] M. Gu, I. Belharouak, J.M. Zheng, H.M. Wu, J. Xiao, A. Genc, K. Amine, S. Thevuthasan, D.R. Baer, J.G. Zhang, N.D. Browning, J. Liu, C.M. Wang, ACS Nano 7 (2013) 760–767.
[8] J.C. Pramudita, D. Pontiroli, G. Magnani, M. Gaboardi, M. Ricco, C. Milanese, H.E.A. Brand, N. Sharma, Chemelectrochem 2 (2015) 600–610.
[9] C. Grosjean, P.H. Miranda, M. Perrin, P. Poggi, Renew. Sustain. Energy Rev. 16 (2012) 1735–1744.
[10] A. Ponrouch, A.R. Goñi, M.R. Palacín, Electrochem. Commun. 27 (2013) 85–88.
[11] Z.H. Wang, L. Qie, L.X. Yuan, W.X. Zhang, X.L. Hu, Y.H. Huang, Carbon 55 (2013) 328–334.
[12] Z. Shadike, Y.-N. Zhou, F. Ding, L. Sang, K.-W. Nam, X.-Q. Yang, Z.-W. Fu, J. Power Sources 260 (2014) 72–76.
[13] Y. Xu, E. Memarzadeh Lotfabad, H. Wang, B. Farbod, Z. Xu, A. Kohandehghan, D. Mitlin, Chem. Commun. 49 (2013) 8973–8975.
[14] Y. Sun, L. Zhao, H. Pan, X. Lu, L. Gu, Y.-S. Hu, H. Li, M. Armand, Y. Ikuhara, L. Chen, X. Huang, Nat. Commun. 4 (2013) 1870.
[15] P. Senguttuvan, G. Rousse, V. Seznec, J.-M. Tarascon, M.R. Palacín, Chem. Mater. 23 (2011) 4109–4111.
[16] G. Wang, L. Liu, L. Zhang, J. Zhang, Ionics 19 (2013) 689–695.
[17] R. Alcántara, M. Jaraba, P. Lavela, J.L. Tirado, Chem. Mater. 14 (2002) 2847–2848.
[18] S. Hariharan, K. Saravanan, V. Ramar, P. Balaya, Phys. Chem. Chem. Phys. 15 (2013) 2945–2953.
[19] S. Hariharan, K. Saravanan, P. Balaya, Electrochem. Commun. 31 (2013) 5–9.
[20] S. Yuan, X.-l. Huang, D.-l. Ma, H.-g. Wang, F.-z. Meng, X.-b. Zhang, Adv. Mater. 26 (2014) 2273–2279.
[21] H.-S. Ryu, J.-S. Kim, J. Park, J.-Y. Park, G.-B. Cho, X. Liu, I.-S. Ahn, K.-W. Kim, J.-H. Ahn, J.-P. Ahn, S.W. Martin, G. Wang, H.-J. Ahn, J. Power Sources 244 (2013) 764–770.
[22] T. Zhou, W.K. Pang, C. Zhang, J. Yang, Z. Chen, H.K. Liu, Z. Guo, ACS Nano 8 (2014) 8323–8333.
[23] Q. Su, G. Du, J. Zhang, Y. Zhong, B. Xu, Y. Yang, S. Neupane, W. Li, ACS Nano 8 (2014) 3620–3627.
[24] J. Qian, X. Wu, Y. Cao, X. Ai, H. Yang, Angew. Chem. 125 (2013) 4731–4734.
[25] Y. Kim, Y. Kim, A. Choi, S. Woo, D. Mok, N.-S. Choi, Y.S. Jung, J.H. Ryu, S.M. Oh, K.T. Lee, Adv. Mater. 26 (2014) 4139–4144.
[26] L. Shi, T. Zhao, J. Mater. Chem. 5 (2017) 3735–3758.
[27] J. Mao, T. Zhou, Y. Zheng, H. Gao, H.k. Liu, Z. Guo, J. Mater. Chem. 6 (2018) 3284–3303.
[28] Y. Wu, Y. Yu, Energy Stor. Mater. 16 (2019) 323–343.
[29] H.G. Wang, Z. Wu, F.L. Meng, D.L. Ma, X.L. Huang, L.M. Wang, X.B. Zhang, ChemSusChem 6 (2013) 56–60.
[30] X. Zheng, X. Li, Z. Huang, B. Zhang, Z. Wang, H. Guo, Z. Yang, J. Alloys Compd. 644 (2015) 607–614.
[31] J. Yang, X. Zhou, D. Wu, X. Zhao, Z. Zhou, Adv. Mater. 29 (2017).
[32] X. Xu, H. Zeng, D. Han, K. Qiao, W. Xing, M.J. Rood, Z. Yan, ACS Appl. Mater. Interfaces 10 (2018) 37172–37180.
[33] T. Yang, T. Qian, M. Wang, X. Shen, N. Xu, Z. Sun, C. Yan, Adv. Mater. 28 (2016) 539–545.
[34] S. Balendhran, S. Walia, H. Nili, J.Z. Ou, S. Zhuiykov, R.B. Kaner, S. Sriram, M. Bhaskaran, K. Kalantar-zadeh, Adv. Funct. Mater. 23 (2013), 3946-3946.
[35] Z. Hu, Q. Liu, S.-L. Chou, S.-X. Dou, Adv. Mater. 29 (2017), 1700606.
[36] S. Kajiyama, L. Szabova, K. Sodeyama, H. Iinuma, R. Morita, K. Gotoh, Y. Tateyama, M. Okubo, A. Yamada, ACS Nano 10 (2016) 3334–3341.
[37] X. Xie, M.-Q. Zhao, B. Anasori, K. Maleski, C.E. Ren, J. Li, B.W. Byles, E. Pomerantseva, G. Wang, Y. Gogotsi, Nano Energy 26 (2016) 513–523.
[38] J. Sun, H.W. Lee, M. Pasta, H. Yuan, G. Zheng, Y. Sun, Y. Li, Y. Cui, Nat. Nanotechnol. 10 (2015) 980–985.
[39] V.V. Kulish, O.I. Malyi, M.-F. Ng, Z. Chen, S. Manzhos, P. Wu, Phys. Chem. Chem. Phys. 16 (2014) 4260–4267.
[40] Q. Li, Z. Li, Z. Zhang, C. Li, J. Ma, C. Wang, X. Ge, S. Dong, L. Yin, Adv. Energy Mater. 6 (2016).
[41] L. Shi, T. Zhao, A. Xu, J. Xu, Sci. Bull. 61 (2016) 1138–1144.
[42] J. Sangster, J. Phase Equilibria Diffus. 28 (2007) 571–579.
[43] Z. Wang, L. Qie, L. Yuan, W. Zhang, X. Hu, Y. Huang, Carbon 55 (2013) 328–334.
[44] R. Alcántara, J.M. Jiménez-Mateos, P. Lavela, J.L. Tirado, Electrochem. Commun. 3 (2001) 639–642.
[45] K. Tang, L. Fu, R.J. White, L. Yu, M.-M. Titirici, M. Antonietti, J. Maier, Adv. Energy Mater. 2 (2012) 873–877.
[46] Y. Cao, L. Xiao, M.L. Sushko, W. Wang, B. Schwenzer, J. Xiao, Z. Nie, L.V. Saraf, Z. Yang, J. Liu, Nano Lett. 12 (2012) 3783–3787.
[47] J. Liu, X.W. Liu, Adv. Mater. 24 (2012) 4097–4111.
[48] X. Huang, X. Qi, F. Boey, H. Zhang, Chem. Soc. Rev. 41 (2012) 666–686.
[49] Y.-X. Wang, S.-L. Chou, H.-K. Liu, S.-X. Dou, Carbon 57 (2013) 202–208.
[50] A.K. Geim, K.S. Novoselov, The rise of graphene, in: Nanoscience and Technology: A Collection of Reviews from Nature Journals, World Scientific, 2010, pp. 11–19.
[51] S. Yang, X. Feng, X. Wang, K. Müllen, Angew. Chem. Int. Ed. 50 (2011) 5339–5343.

[52] Q. Cheng, J. Tang, J. Ma, H. Zhang, N. Shinya, L.-C. Qin, Phys. Chem. Chem. Phys. 13 (2011) 17615–17624.
[53] M. Pumera, Energy Environ. Sci. 4 (2011) 668–674.
[54] L. Qie, W. Chen, X. Xiong, C. Hu, F. Zou, P. Hu, Y. Huang, Adv. Sci. (2015) 2.
[55] B. Quan, A. Jin, S.H. Yu, S.M. Kang, J. Jeong, H.D. Abruña, L. Jin, Y. Piao, Y.E. Sung, Adv. Sci. 5 (2018), 1700880.
[56] D. Datta, J. Li, V.B. Shenoy, ACS Appl. Mater. Interfaces 6 (2014) 1788–1795.
[57] Y. Wang, C. Wang, Y. Wang, H. Liu, Z. Huang, ACS Appl. Mater. Interfaces 8 (2016) 18860–18866.
[58] J. Xu, M. Wang, N.P. Wickramaratne, M. Jaroniec, S. Dou, L. Dai, Adv. Mater. 27 (2015) 2042–2048.
[59] X. Wang, G. Li, F.M. Hassan, J. Li, X. Fan, R. Batmaz, X. Xiao, Z. Chen, Nano Energy 15 (2015) 746–754.
[60] M.S. Whittingham, Prog. Solid State Chem. 12 (1978) 41–99.
[61] X. Wang, X. Shen, Z. Wang, R. Yu, L. Chen, ACS Nano 8 (2014) 11394–11400.
[62] Y. Zhu, P. Nie, L. Shen, S. Dong, Q. Sheng, H. Li, H. Luo, X. Zhang, Nanoscale 7 (2015) 3309–3315.
[63] Y.W. Denis, P.V. Prikhodchenko, C.W. Mason, S.K. Batabyal, J. Gun, S. Sladkevich, A.G. Medvedev, O. Lev, Nat. Commun. 4 (2013) 2922.
[64] B. Lu, Y. Song, Q. Zhang, J. Pan, Y.-T. Cheng, J. Zhang, Phys. Chem. Chem. Phys. 18 (2016) 4721–4727.
[65] Z. Hu, K. Zhang, Z. Zhu, Z. Tao, J. Chen, J. Mater. Chem. 3 (2015) 12898–12904.
[66] K. Zhang, M. Park, L. Zhou, G.H. Lee, J. Shin, Z. Hu, S.L. Chou, J. Chen, Y.M. Kang, Angew Chem. Int. Ed. Engl. 55 (2016) 12822–12826.
[67] S.-H. Yu, S.H. Lee, D.J. Lee, Y.-E. Sung, T. Hyeon, Small 12 (2016) 2146–2172.
[68] F. Klein, B. Jache, A. Bhide, P. Adelhelm, Phys. Chem. Chem. Phys. 15 (2013) 15876–15887.
[69] D.Y. Yu, P.V. Prikhodchenko, C.W. Mason, S.K. Batabyal, J. Gun, S. Sladkevich, A.G. Medvedev, O. Lev, Nat. Commun. 4 (2013) 2922.
[70] Y. Zhao, A. Manthiram, Chem. Commun. (Camb) 51 (2015) 13205–13208.
[71] X. Xiong, G. Wang, Y. Lin, Y. Wang, X. Ou, F. Zheng, C. Yang, J.H. Wang, M. Liu, ACS Nano 10 (2016) 10953–10959.
[72] Z. Hu, L. Wang, K. Zhang, J. Wang, F. Cheng, Z. Tao, J. Chen, Angew Chem. Int. Ed. Engl. 53 (2014) 12794–12798.
[73] S.H. Choi, Y.N. Ko, J.-K. Lee, Y.C. Kang, Adv. Funct. Mater. 25 (2015) 1780–1788.
[74] Y. Li, Y. Liang, F.C. Robles Hernandez, H. Deog Yoo, Q. An, Y. Yao, Nano Energy 15 (2015) 453–461.
[75] D. Su, S. Dou, G. Wang, Adv. Energy Mater. 5 (2015) 1401205.
[76] Y. Liu, X. He, D. Hanlon, A. Harvey, J.N. Coleman, Y. Li, ACS Nano 10 (2016) 8821–8828.
[77] T.S. Sahu, Q. Li, J. Wu, V.P. Dravid, S. Mitra, J. Mater. Chem. 5 (2017) 355–363.
[78] H. Yang, M. Wang, X. Liu, Y. Jiang, Y. Yu, Nano Res. 11 (2018) 3844–3853.
[79] S.H. Choi, Y.C. Kang, Nanoscale 7 (2015) 3965–3970.
[80] Y. Wang, D. Kong, W. Shi, B. Liu, G.J. Sim, Q. Ge, H.Y. Yang, Adv. Energy Mater. 6 (2016).
[81] B. Qu, C. Ma, G. Ji, C. Xu, J. Xu, Y.S. Meng, T. Wang, J.Y. Lee, Adv. Mater. 26 (2014) 3854–3859.
[82] P.V. Prikhodchenko, D.Y.W. Yu, S.K. Batabyal, V. Uvarov, J. Gun, S. Sladkevich, A.A. Mikhaylov, A.G. Medvedev, O. Lev, J. Mater. Chem. (2014) 2.
[83] Y. Liu, H. Kang, L. Jiao, C. Chen, K. Cao, Y. Wang, H. Yuan, Nanoscale 7 (2015) 1325–1332.
[84] Y. Zhang, P. Zhu, L. Huang, J. Xie, S. Zhang, G. Cao, X. Zhao, Adv. Funct. Mater. 25 (2015) 481–489.
[85] W. Sun, X. Rui, D. Yang, Z. Sun, B. Li, W. Zhang, Y. Zong, M. Srinivasan, S. Dou, Q. Yan, ACS Nano 9 (2015) 11371–11381.
[86] P. Zhou, X. Wang, W. Guan, D. Zhang, L. Fang, Y. Jiang, ACS Appl. Mater. Interfaces 9 (2017) 6979–6987.
[87] S.H. Choi, Y.C. Kang, Nano Res. 8 (2015) 1595–1603.
[88] Y.C. Lu, C. Ma, J. Alvarado, N. Dimov, Y.S. Meng, S. Okada, J. Mater. Chem. 3 (2015) 16971–16977.
[89] D. Chao, C. Zhu, P. Yang, X. Xia, J. Liu, J. Wang, X. Fan, S.V. Savilov, J. Lin, H.J. Fan, Z.X. Shen, Nat. Commun. 7 (2016) 12122.
[90] Y. Zheng, T. Zhou, C. Zhang, J. Mao, H. Liu, Z. Guo, Angew Chem. Int. Ed. Engl. 55 (2016) 3408–3413.
[91] C. Xia, F. Zhang, H. Liang, H.N. Alshareef, Nano Res. 10 (2017) 4368–4377.
[92] X. Xiong, C. Yang, G. Wang, Y. Lin, X. Ou, J.-H. Wang, B. Zhao, M. Liu, Z. Lin, K. Huang, Energy Environ. Sci. 10 (2017) 1757–1763.
[93] W. Ren, H. Zhang, C. Guan, C. Cheng, Adv. Funct. Mater. 27 (2017) 1702116.
[94] Y.X. Wang, J. Yang, S.L. Chou, H.K. Liu, W.X. Zhang, D. Zhao, S.X. Dou, Nat. Commun. 6 (2015) 8689.
[95] Z. Hu, Z. Zhu, F. Cheng, K. Zhang, J. Wang, C. Chen, J. Chen, Energy Environ. Sci. 8 (2015) 1309–1316.
[96] Z. Liu, T. Lu, T. Song, X.-Y. Yu, X.W. Lou, U. Paik, Energy Environ. Sci. 10 (2017) 1576–1580.
[97] X. Xu, S. Ji, M. Gu, J. Liu, ACS Appl. Mater. Interfaces 7 (2015) 20957–20964.
[98] D. Yu, Q. Pang, Y. Gao, Y. Wei, C. Wang, G. Chen, F. Du, Energy Stor. Mater. 11 (2018) 1–7.
[99] J. Zhou, L. Wang, M. Yang, J. Wu, F. Chen, W. Huang, N. Han, H. Ye, F. Zhao, Y. Li, Y. Li, Adv. Mater. 29 (2017).
[100] R. Sun, Q. Wei, Q. Li, W. Luo, Q. An, J. Sheng, D. Wang, W. Chen, L. Mai, ACS Appl. Mater. Interfaces 7 (2015) 20902–20908.
[101] S. Peng, X. Han, L. Li, Z. Zhu, F. Cheng, M. Srinivansan, S. Adams, S. Ramakrishna, Small 12 (2016) 1359–1368.
[102] T. Chen, Y. Ma, Q. Guo, M. Yang, H. Xia, J. Mater. Chem. 5 (2017) 3179–3185.
[103] G. Suo, D. Li, L. Feng, X. Hou, Q. Yu, Y. Yang, W. Wang, Mater. Lett. 236 (2019) 312–315.
[104] X. Wang, Y. Chen, Y. Fang, J. Zhang, S. Gao, X.W.D. Lou, Angew Chem. Int. Ed. Engl. 58 (2019) 2675–2679.
[105] H. Li, K. Wang, S. Cheng, K. Jiang, ACS Appl. Mater. Interfaces 10 (2018) 8016–8025.
[106] T. Wang, P. Hu, C. Zhang, H. Du, Z. Zhang, X. Wang, S. Chen, J. Xiong, G. Cui, ACS Appl. Mater. Interfaces 8 (2016) 7811–7817.
[107] Z. Chen, W. Ren, L. Gao, B. Liu, S. Pei, H.-M. Cheng, Nat. Mater. 10 (2011) 424–428.
[108] B.G. Choi, M. Yang, W.H. Hong, J.W. Choi, Y.S. Huh, ACS Nano 6 (2012) 4020–4028.
[109] J. Luo, J. Kim, J. Huang, Acc. Chem. Res. 46 (2013) 2225–2234.
[110] C. Li, G. Shi, Nanoscale 4 (2012) 5549–5563.
[111] X. Cao, B. Zheng, X. Rui, W. Shi, Q. Yan, H. Zhang, Angew. Chem. Int. Ed. 53 (2014) 1404–1409.
[112] S.H. Choi, Y.C. Kang, ChemSusChem 7 (2014) 523–528.
[113] Y. Huang, D. Wu, J. Wang, S. Han, L. Lv, F. Zhang, X. Feng, Small 10 (2014) 2226–2232.
[114] G. Fang, Z. Wu, J. Zhou, C. Zhu, X. Cao, T. Lin, Y. Chen, C. Wang, A. Pan, S. Liang, Adv. Energy Mater. 8 (2018).
[115] S. Liu, W. Lei, Y. Liu, Q. Qiao, W.-H. Zhang, ACS Appl. Mater. Interfaces 10 (2018) 37445–37452.
[116] Y. Von Lim, S. Huang, Y. Zhang, D. Kong, Y. Wang, L. Guo, J. Zhang, Y. Shi, T.P. Chen, L.K. Ang, H.Y. Yang, Energy Stor. Mater. 15 (2018) 98–107.
[117] J. Lv, D. Bai, L. Yang, Y. Guo, H. Yan, S. Xu, Chem. Commun. (Camb) 54 (2018) 8909–8912.
[118] S. Wang, Y. Yang, W. Quan, Y. Hong, Z. Zhang, Z. Tang, J. Li, Nano Energy 32 (2017) 294–301.
[119] Z. Chen, V. Augustyn, X. Jia, Q. Xiao, B. Dunn, Y. Lu, ACS Nano 6 (2012) 4319–4327.
[120] S. Lou, X. Cheng, Y. Zhao, A. Lushington, J. Gao, Q. Li, P. Zuo, B. Wang, Y. Gao, Y. Ma, C. Du, G. Yin, X. Sun, Nano Energy 34 (2017) 15–25.
[121] X.Y. Yu, X.W. Lou, Adv. Energy Mater. 8 (2018) 1701592.
[122] X. Xie, Z. Ao, D. Su, J. Zhang, G. Wang, Adv. Funct. Mater. 25 (2015) 1393–1403.
[123] Y. Jiang, M. Wei, J. Feng, Y. Ma, S. Xiong, Energy Environ. Sci. 9 (2016) 1430–1438.
[124] D. Chao, P. Liang, Z. Chen, L. Bai, H. Shen, X. Liu, X. Xia, Y. Zhao, S.V. Savilov, J. Lin, Z.X. Shen, ACS Nano 10 (2016) 10211–10219.
[125] Q. Wang, W. Zhang, C. Guo, Y. Liu, C. Wang, Z. Guo, Adv. Funct. Mater. (2017) 27.
[126] Z. Wei, L. Wang, M. Zhuo, W. Ni, H. Wang, J. Ma, J. Mater. Chem. 6 (2018) 12185–12214.
[127] Y.N. Ko, S.H. Choi, S.B. Park, Y.C. Kang, Nanoscale 6 (2014) 10511–10515.
[128] L. Ma, X. Zhou, L. Xu, X. Xu, L. Zhang, W. Chen, J. Power Sources 285 (2015) 274–280.
[129] Z. Zhang, X. Yang, Y. Fu, K. Du, J. Power Sources 296 (2015) 2–9.
[130] Y. Tang, Z. Zhao, Y. Wang, Y. Dong, Y. Liu, X. Wang, J. Qiu, ACS Appl. Mater. Interfaces 8 (2016) 32324–32332.
[131] Z. Ali, M. Asif, X. Huang, T. Tang, Y. Hou, Adv. Mater. 30 (2018) 1802745.
[132] Q. Tang, Y. Cui, J. Wu, D. Qu, A.P. Baker, Y. Ma, X. Song, Y. Liu, Nano Energy 41 (2017) 377–386.
[133] Y. Fang, X.Y. Yu, X.W. Lou, Adv. Mater. 30 (2018) 1706668.
[134] J.-S. Park, Y. Chan Kang, J. Mater. Chem. 5 (2017) 8616–8623.
[135] F. Zhang, C. Xia, J. Zhu, B. Ahmed, H. Liang, D.B. Velusamy, U. Schwingenschlögl, H.N. Alshareef, Adv. Energy Mater. 6 (2016) 1601188.
[136] S. Yuan, Y.H. Zhu, W. Li, S. Wang, D. Xu, L. Li, Y. Zhang, X.B. Zhang, Adv. Mater. 29 (2017).
[137] K. Zhang, Z. Hu, X. Liu, Z. Tao, J. Chen, Adv. Mater. 27 (2015) 3305–3309.
[138] H. Fan, H. Yu, Y. Zhang, J. Guo, Z. Wang, H. Wang, N. Zhao, Y. Zheng, C. Du, Z. Dai, Q. Yan, J. Xu, Energy Stor. Mater. 10 (2018) 48–55.
[139] J.H. Choi, S.K. Park, Y.C. Kang, Small 15 (2019), e1803043.
[140] K. Zhang, M. Park, L. Zhou, G.-H. Lee, W. Li, Y.-M. Kang, J. Chen, Adv. Funct. Mater. 26 (2016) 6728–6735.
[141] Z. Ali, T. Tang, X. Huang, Y. Wang, M. Asif, Y. Hou, Energy Stor. Mater. 13 (2018) 19–28.
[142] X. Ou, C. Yang, X. Xiong, F. Zheng, Q. Pan, C. Jin, M. Liu, K. Huang, Adv. Funct. Mater. 27 (2017) 1606242.
[143] X. Yang, J. Zhang, Z. Wang, H. Wang, C. Zhi, D.Y.W. Yu, A.L. Rogach, Small 14 (2018) 1702669.
[144] M. Xu, F. Yi, Y. Niu, J. Xie, J. Hou, S. Liu, W. Hu, Y. Li, C.M. Li, J. Mater. Chem. 3 (2015) 9932–9937.
[145] J. Zhao, X. Yu, Z. Gao, W. Zhao, R. Xu, Y. Liu, H. Shen, Chem. Eng. J. 332 (2018) 548–555.
[146] L.-Q. Sun, M.-J. Li, K. Sun, S.-H. Yu, R.-S. Wang, H.-M. Xie, J. Phys. Chem. C 116 (2012) 14772–14779.
[147] L. Wang, X. He, J. Li, W. Sun, J. Gao, J. Guo, C. Jiang, Angew. Chem. Int. Ed. 51 (2012) 9034–9037.
[148] Y. Kim, Y. Park, A. Choi, N.-S. Choi, J. Kim, J. Lee, J.H. Ryu, S.M. Oh, K.T. Lee, Adv. Mater. 25 (2013) 3045–3049.
[149] H. Liu, A.T. Neal, Z. Zhu, Z. Luo, X. Xu, D. Tománek, P.D. Ye, ACS Nano 8 (2014) 4033–4041.
[150] H.O.H. Churchill, P. Jarillo-Herrero, Nat. Nanotechnol. 9 (2014) 330.

[151] R. Hultgren, N.S. Gingrich, B.E. Warren, J. Chem. Phys. 3 (1935) 351–355.
[152] G.E. Bacon, Acta Crystallogr. 4 (1951) 558–561.
[153] K.P.S.S. Hembram, H. Jung, B.C. Yeo, S.J. Pai, S. Kim, K.-R. Lee, S.S. Han, J. Phys. Chem. C 119 (2015) 15041–15046.
[154] C.M. Park, H.J. Sohn, Adv. Mater. 19 (2007) 2465–2468.
[155] M. Nagao, A. Hayashi, M. Tatsumisago, J. Power Sources 196 (2011) 6902–6905.
[156] J. Sun, G. Zheng, H.-W. Lee, N. Liu, H. Wang, H. Yao, W. Yang, Y. Cui, Nano Lett. 14 (2014) 4573–4580.
[157] C. Chowdhury, S. Karmakar, A. Datta, ACS Energy Lett. 1 (2016) 253–259.
[158] H.W. Lee, H. Jung, B.C. Yeo, D. Kim, S.S. Han, J. Phys. Chem. C 122 (2018) 20653–20660.
[159] X. Fan, J. Mao, Y. Zhu, C. Luo, L. Suo, T. Gao, F. Han, S.-C. Liou, C. Wang, Adv. Energy Mater. 5 (2015).
[160] J. Mao, X. Fan, C. Luo, C. Wang, ACS Appl. Mater. Interfaces 8 (2016) 7147–7155.
[161] C. Wu, P. Kopold, P.A. van Aken, J. Maier, Y. Yu, Adv. Mater. 29 (2017).
[162] X. Ge, Z. Li, L. Yin, Nano Energy 32 (2017) 117–124.
[163] W.-J. Li, Q.-R. Yang, S.-L. Chou, J.-Z. Wang, H.-K. Liu, J. Power Sources 294 (2015) 627–632.
[164] X. Wang, K. Chen, G. Wang, X. Liu, H. Wang, ACS Nano 11 (2017) 11602–11616.
[165] W.-J. Li, S.-L. Chou, J.-Z. Wang, H.-K. Liu, S.-X. Dou, Chem. Commun. 51 (2015) 3682–3685.
[166] J. Qian, Y. Xiong, Y. Cao, X. Ai, H. Yang, Nano Lett. 14 (2014) 1865–1869.
[167] W. Zhang, J. Mao, W.K. Pang, Z. Guo, Z. Chen, Electrochim. Acta 235 (2017) 107–113.
[168] Z. Huang, H. Hou, Y. Zhang, C. Wang, X. Qiu, X. Ji, Adv. Mater. 29 (2017).
[169] X.W. Wang, H.P. Guo, J. Liang, J.F. Zhang, B. Zhang, J.Z. Wang, W.B. Luo, H.K. Liu, S.X. Dou, Adv. Funct. Mater. 28 (2018) 1801016.
[170] M. Naguib, V.N. Mochalin, M.W. Barsoum, Y. Gogotsi, Adv. Mater. 26 (2014) 992–1005.
[171] M. Naguib, Y. Gogotsi, Acc. Chem. Res. 48 (2015) 128–135.
[172] X. Liang, A. Garsuch, L.F. Nazar, Angew. Chem. Int. Ed. 54 (2015) 3907–3911.
[173] D. Er, J. Li, M. Naguib, Y. Gogotsi, V.B. Shenoy, ACS Appl. Mater. Interfaces 6 (2014) 11173–11179.
[174] M.R. Lukatskaya, S. Kota, Z. Lin, M.-Q. Zhao, N. Shpigel, M.D. Levi, J. Halim, P.-L. Taberna, M.W. Barsoum, P. Simon, Y. Gogotsi, Nat. Energy 2 (2017) 17105.
[175] M.-Q. Zhao, M. Torelli, C.E. Ren, M. Ghidiu, Z. Ling, B. Anasori, M.W. Barsoum, Y. Gogotsi, Nano Energy 30 (2016) 603–613.
[176] D. Zhao, R. Zhao, S. Dong, X. Miao, Z. Zhang, C. Wang, L. Yin, Energy Environ. Sci. 12 (2019) 2422–2432.
[177] S. Sun, Z. Xie, Y. Yan, S. Wu, Chem. Eng. J. 366 (2019) 460–467.
[178] Y. Wu, P. Nie, L. Wu, H. Dou, X. Zhang, Chem. Eng. J. 334 (2018) 932–938.
[179] R. Meng, J. Huang, Y. Feng, L. Zu, C. Peng, L. Zheng, L. Zheng, Z. Chen, G. Liu, B. Chen, Y. Mi, J. Yang, Adv. Energy Mater. 8 (2018).
[180] P. Lian, Y. Dong, Z.-S. Wu, S. Zheng, X. Wang, W. Sen, C. Sun, J. Qin, X. Shi, X. Bao, Nano Energy 40 (2017) 1–8.
[181] M.Q. Zhao, X. Xie, C.E. Ren, T. Makaryan, B. Anasori, G. Wang, Y. Gogotsi, Adv. Mater. 29 (2017) 1702410.
[182] S.M. Bak, R. Qiao, W. Yang, S. Lee, X. Yu, B. Anasori, H. Lee, Y. Gogotsi, X.Q. Yang, Adv. Energy Mater. 7 (2017) 1700959.
[183] X. Xie, K. Kretschmer, B. Anasori, B. Sun, G. Wang, Y. Gogotsi, ACS Appl. Nano Mater. 1 (2018) 505–511.
[184] V. Natu, M. Clites, E. Pomerantseva, M.W. Barsoum, Mater. Res. Lett. 6 (2018) 230–235.
[185] X. Wang, X. Shen, Y. Gao, Z. Wang, R. Yu, L. Chen, J. Am. Chem. Soc. 137 (2015) 2715–2721.
[186] L.F. Huang, M.J. Hutchison, R.J. Santucci, J.R. Scully, J.M. Rondinelli, J. Phys. Chem. C 121 (2017) 9782–9789.
[187] S. Cahangirov, M. Topsakal, E. Aktürk, H. Şahin, S. Ciraci, Phys. Rev. Lett. 102 (2009) 236804.
[188] M.E. Dávila, L. Xian, S. Cahangirov, A. Rubio, G. Le Lay, New J. Phys. 16 (2014), 095002.
[189] B. Mortazavi, A. Dianat, G. Cuniberti, T. Rabczuk, Electrochim. Acta 213 (2016) 865–870.
[190] A.J. Mannix, X.-F. Zhou, B. Kiraly, J.D. Wood, D. Alducin, B.D. Myers, X. Liu, B.L. Fisher, U. Santiago, J.R. Guest, M.J. Yacaman, A. Ponce, A.R. Oganov, M.C. Hersam, N.P. Guisinger, Science 350 (2015) 1513.
[191] C. Uthaisar, V. Barone, Nano Lett. 10 (2010) 2838–2842.
[192] Y. Jing, Z. Zhou, C.R. Cabrera, Z. Chen, J. Phys. Chem. C 117 (2013) 25409–25413.
[193] L. Shi, T.S. Zhao, A. Xu, J.B. Xu, J. Mater. Chem. 4 (2016) 16377–16382.
[194] H. Nishino, T. Fujita, N.T. Cuong, S. Tominaka, M. Miyauchi, S. Iimura, A. Hirata, N. Umezawa, S. Okada, E. Nishibori, A. Fujino, T. Fujimori, S.-i. Ito, J. Nakamura, H. Hosono, T. Kondo, J. Am. Chem. Soc. 139 (2017) 13761–13769.
[195] M. Makaremi, B. Mortazavi, C.V. Singh, Mater. Today Energy 8 (2018) 22–28.
[196] Y. Yang, X. Liu, Z. Zhu, Y. Zhong, Y. Bando, D. Golberg, J. Yao, X. Wang, Joule 2 (2018) 1075–1094.
[197] G. Zhang, T. Xiong, L. He, M. Yan, K. Zhao, X. Xu, L. Mai, J. Mater. Sci. 52 (2017) 3697–3718.
[198] D.J. Hynek, J.V. Pondick, J.J. Cha, Apl. Mater. 7 (2019), 030902.
[199] Z. Shadike, E. Zhao, Y.-N. Zhou, X. Yu, Y. Yang, E. Hu, S. Bak, L. Gu, X.-Q. Yang, Adv. Energy Mater. 8 (2018) 1702588.
[200] S. Li, Z. Zhao, C. Li, Z. Liu, D. Li, Nano-Micro Lett. 11 (2019) 14.
[201] C. Yang, X. Ou, X. Xiong, F. Zheng, R. Hu, Y. Chen, M. Liu, K. Huang, Energy Environ. Sci. 10 (2017) 107–113.
[202] X. Ou, X. Xiong, F. Zheng, C. Yang, Z. Lin, R. Hu, C. Jin, Y. Chen, M. Liu, J. Power Sources 325 (2016) 410–416.
[203] X. Ou, J. Li, F. Zheng, P. Wu, Q. Pan, X. Xiong, C. Yang, M. Liu, J. Power Sources 343 (2017) 483–491.
[204] X. Ou, X. Liang, F. Zheng, P. Wu, Q. Pan, X. Xiong, C. Yang, M. Liu, Electrochim. Acta 258 (2017) 1387–1396.
[205] Z. Ali, M. Asif, T. Zhang, X. Huang, Y. Hou, Small (2019) 1901995, 0.
[206] X. Xie, T. Makaryan, M. Zhao, K.L. Van Aken, Y. Gogotsi, G. Wang, Adv. Energy Mater. 6 (2016) 1502161.
[207] C. Lane, D. Cao, H. Li, Y. Jiao, B. Barbiellini, A. Bansil, H. Zhu, Condens. Matter 4 (2019) 53.
[208] S. Kim, J. Cui, V.P. Dravid, K. He, Adv. Mater. 31 (2019) 1904623.
[209] P. Gao, Y.-Y. Zhang, L. Wang, S. Chen, Y. Huang, X. Ma, K. Liu, D. Yu, Nano Energy 32 (2017) 302–309.
[210] P. Gao, L. Wang, Y. Zhang, Y. Huang, K. Liu, ACS Nano 9 (2015) 11296–11301.
[211] L. Zhang, Y. Tang, Y. Wang, Y. Duan, D. Xie, C. Wu, L. Cui, Y. Li, X. Ning, Z. Shan, RSC Adv. 6 (2016) 96035–96038.
[212] S. Yao, J. Cui, Z. Lu, Z.-L. Xu, L. Qin, J. Huang, Z. Sadighi, F. Ciucci, J.-K. Kim, Adv. Energy Mater. 7 (2017) 1602149.
[213] S.D. Lacey, J. Wan, A.v.W. Cresce, S.M. Russell, J. Dai, W. Bao, K. Xu, L. Hu, Nano Lett. 15 (2015) 1018–1024.
[214] H.M. Cho, M.V. Chen, A.C. MacRae, Y.S. Meng, ACS Appl. Mater. Interfaces 7 (2015) 16231–16239.
[215] J. Wang, L. Wang, C. Eng, J. Wang, Adv. Energy Mater. 7 (2017) 1602706.
[216] C. Zhao, Y. Lu, Y. Li, L. Jiang, X. Rong, Y.-S. Hu, H. Li, L. Chen, Small Methods 1 (2017) 1600063.
[217] S. Wang, X.-B. Zhang, Adv. Mater. 31 (2019) 1805432.